Modeling Porosity Evolution Throughout Reaction-Induced Fracturing in Rocks With Implications for Serpentinization

Lingran Zhang, Christina Nasika, Frédéric-victor Donzé, Xiaojiao Zheng, François Renard, Luc Scholtes

AGU100 ADVANCING EARTH AND SPACE SCIENCE

JGR Solid Earth

RESEARCH ARTICLE
10.1029/2018JB016872

Key Points:
- Development of a numerical model enables to reproduce the porosity pulse observed during hydration reaction
- During serpentinization, the amplitude of the porosity pulse and the duration of this pulse depend on the temperature
- Competing processes exist during the migration of native dihydrogen that forms during serpentinization

Supporting Information:
- Supporting Information S1
- Movie S1
- Movie S2
- Movie S3
- Movie S4
- Movie S5
- Movie S6

Correspondence to:
L. Zhang,
lingran.zhang@univ-grenoble-alpes.fr

Citation:
Zhang, L., Nasika, C., Donzé, F.-V., Zheng, X., Renard, F., & Scholtès, L. (2019). Modeling porosity evolution throughout reaction-induced fracturing in rocks with implications for serpentinization. *Journal of Geophysical Research: Solid Earth*, *124*, 5708–5733. https://doi.org/10.1029/2018JB016872

Received 14 OCT 2018
Accepted 30 MAY 2019
Accepted article online 6 JUN 2019
Published online 29 JUN 2019

Modeling Porosity Evolution Throughout Reaction-Induced Fracturing in Rocks With Implications for Serpentinization

Lingran Zhang[1], Christina Nasika[1], Frédéric-Victor Donzé[1], Xiaojiao Zheng[2], François Renard[1,2], and Luc Scholtès[3]

[1]Univ. Grenoble Alpes, Univ. Savoie Mont Blanc, CNRS, IRD, IFSTTAR, ISTerre, 38000, Grenoble, France, [2]The Njord Centre, Department of Geosciences, University of Oslo, Oslo, Norway, [3]Université de Lorraine, CNRS, GeoRessources, Nancy, France

Abstract Numerical modeling based on the discrete element method was used to explore the kinetics and mechanics of fractures induced by mineral volumetric expansion during rock hydration. Two systems were considered: the hydration of periclase into brucite and the hydration of peridotite into serpentine. We modeled the coupling between mineral transformation, stress, volume increase, and deformation by simulating the volumetric growth of discrete elements based upon an Avrami-type kinetics equation. The model was implemented to consider the effects of stress and temperature on reaction kinetics as well as the alteration of material properties during hydration reactions. We were able to reproduce experimental evidences observed during the transformation of periclase into brucite, including volume growth, fracturing of periclase, formation of a porosity pulse, as well as the slow-down effect of effective stress on the kinetics of the transformation. The model was also applied to study the serpentinization process. We estimated a bell-shaped relationship between temperature and reaction rate of peridotite transformation following observations made during serpentinization experiments. For both periclase and peridotite systems, we characterized a relationship between the formation of a porosity pulse and the rate of fracture development within the medium. During serpentinization, the amplitude of the porosity pulse and the duration of this pulse depend on the reaction rate and, therefore, on the temperature. Our investigations provide geomechanical explanations on how native dihydrogen formed during serpentinization can be expelled and initiates its migration process.

1. Introduction

Reaction-induced fracturing is observed in many geodynamic and engineering contexts, from salt damage in concrete and rocks (Flatt, 2002; Noiriel et al., 2012; Steiger, 2005), formation of travertine deposits (Gratier et al., 2012), rock weathering (Røyne et al., 2008), and hydration reactions in the Earth's crust, including serpentinization and eclogitization transformations (Iyer et al., 2008; Jamtveit, Malthe-Sørenssen, & Kostenko, 2008; Kelemen & Hirth, 2012; Lafay et al., 2018; Lisabeth et al., 2017; Martin & Fyfe, 1970). Serpentinization occurs when mafic rocks originating from the Earth's mantle or crust, such as peridotites and volcanic rocks, are uplifted in the crust and meet meteoric or oceanic waters. These rocks undergo changes in pressure and temperature conditions, which cause them to react in presence of water and produce fracturing, with microseismicity (Horning et al., 2018; Schlindwein & Schmid, 2016). This process has major geodynamical consequences, such as modifying the frictional properties of tectonic plate boundaries, recycling water in the crust, and providing local environments where life could develop (e.g., Guillot et al., 2015). It also produces significant amounts of molecular dihydrogen H_2 (Bogdanov et al., 1995; Charlou et al., 2002; Foustoukos et al., 2008; Früh-Green et al., 2003; Kelley et al., 2005; Moody, 1976; Proskurowski et al., 2008). Field measurements have actually shown that sources of this native hydrogen exist on the Earth's surface (Guélard et al., 2017; Larin et al., 2010; Larin et al., 2014).

Several approaches have been proposed to model reaction-induced fracturing. Kelemen and Hirth (2012) developed thermodynamic and mineral physics estimates of the crystallization pressure and differential stress resulting from volume changes during olivine hydration (serpentinization) and carbonation. Ulven et al. (2014) studied the deformation and fracture mechanisms in a simplified system using a range of numerical techniques and found that the sharpness of reaction fronts and the magnitude of volume increase were

the main parameters controlling the mode of failure. Ulven et al. (2014) developed a 2-D discrete element model that coupled reaction, fracturing, and fluid transport for systems with a range of initial porosities. They concluded that porosity had a first-order effect on the progress of reaction-driven fracturing during weathering and other volatilization processes in the Earth's crust. Malvoisin et al. (2017) combined numerical modeling (based on a micromechanical model and a simple geometrical model) and observations in natural samples to provide estimates of the serpentinization rate at mid-ocean ridges. Evans et al. (2018) used a poroelastic model and chemical mass balance calculations to derive a system of equations describing reactive fluid flow in elastically deformable porous media. This model was applied to study serpentinization in a subseafloor environment. Their study highlighted the role of surface energy in driving the fluid to access dry/unreacted rock volumes. Skarbek et al. (2018) measured uniaxial reaction-induced stresses generated during gypsum formation via bassanite hydration and found that the stresses generated through solid volume increase were limited by viscous compaction. The observed behavior was explained with a phenomenological model that predicted strain evolution using kinetic relationships for the reaction and creep rates. The application of a similar model to the hydration of olivine also predicted crystallization-induced stresses about an order of magnitude lower than the thermodynamically predicted crystallization pressures (Kelemen & Hirth, 2012) for both the formation of lizardite and antigorite. However, these studies did not take into consideration the alteration of mechanical properties caused by retrograde metamorphism, which has important geodynamic consequences (Guillot et al., 2015) and could also control the migration of native H_2 produced by serpentinization.

In the present study, we develop a numerical model that reproduces two hydration reactions, the hydration of periclase and the hydration of peridotite (serpentinization), by considering the effects of the effective stress and of the temperature on the reaction rate, as well as the modification of the mechanical properties throughout the reaction. First, the model is verified against several experimental results of Zheng et al. (2018) where the hydration of periclase into brucite was monitored at crustal conditions. Then, the model is utilized to gain a better understanding of the porosity pulse observed during the serpentinization process.

2. Background

2.1. Avrami Kinetics, Volume Increase and Fracturing

Reaction-induced fracturing is representative of many reactions that take place during metamorphism (Jamtveit, Malthe-Sørenssen, & Kostenko, 2008; Jamtveit, Putnis, & Malthe-Sørenssen, 2008; Kelemen & Hirth, 2012; MacDonald & Fyfe, 1985; O'Hanley, 1992; Zheng et al., 2018; Zhu et al., 2016). The reaction progress during the hydration of periclase and serpentinization has been described by an Avrami-type relationship (Martin & Fyfe, 1970) and has been measured experimentally (Zheng et al., 2018). Avrami kinetics (Avrami, 1939) describe reactions that occur at a solid reactant surface with numerous sites where the product may nucleate. In Avrami kinetics, the percentage of reaction completion versus time follows a sigmoidal curve (Figure 1a) which can be segmented in three different stages. First, during an incubation period, the product phase nucleates randomly in the volume. In a second stage, the reaction accelerates and the product nuclei grow while new nucleation forms. Finally, in a third stage, a deceleration is observed where the nucleation rate decreases while the growth continues upon completion of the reaction. The Avrami kinetics can be described by the following relation:

$$C = 1 - e^{(-kt^n)} \tag{1}$$

where C is the extent of transformation (the reaction is complete when $C = 1$), t is the time, k is a kinetics parameter related to the rate of the reaction, which is a function of thermodynamic parameters such as temperature and pressure, and n is a function of the number and type of time-dependent processes participating to the reaction (Wegner & Ernst, 1983).

Both hydration of periclase and serpentinization involve significant volume increases due to the lower density of the reaction products. The hydration of periclase can induce a solid volume increase of about 110% at 1 bar and 25 °C (Zheng et al., 2018). The solid volume expansion associated with the hydration of olivine to serpentine may reach a maximum of 50% (Malvoisin et al., 2017). MacDonald and Fyfe (1985) suggested that the volume increase associated with the serpentinization reaction is responsible for the

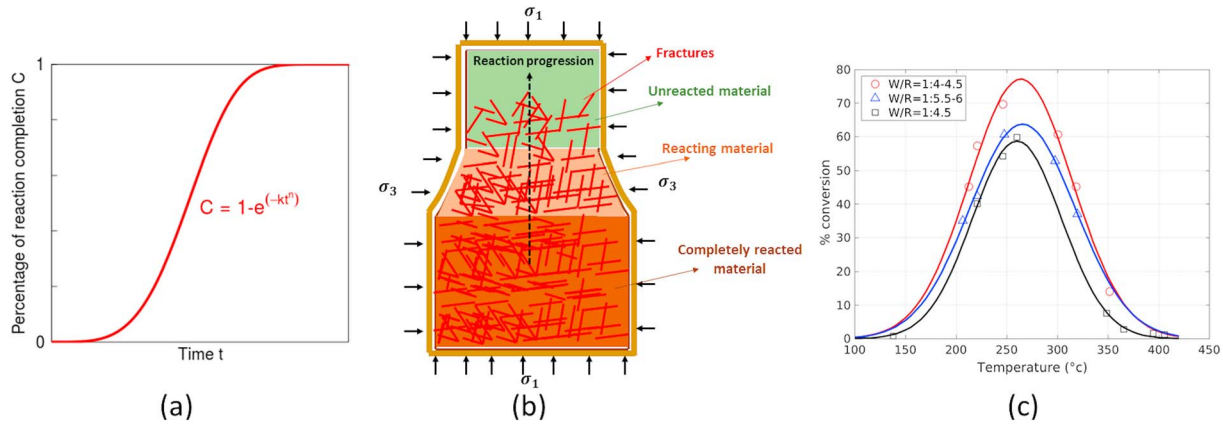

Figure 1. (a) Percentage of reaction completion versus time for an Avrami type reaction kinetics, (b) sketch of the fracturing associated with a hydration reaction with progression of a reaction front, (c) experimental conversion volume versus temperature for synthetic forsterite and olivine powders (data from Martin & Fyfe, 1970). The different curves correspond to different water to rock (W/R) ratios.

formation of a continuous crack network that develops as the reaction proceeds. Such reaction-induced fracturing during olivine hydration and other replacement processes have been observed in several experiments and studied with numerous numerical models (Jamtveit, Putnis, & Malthe-Sørenssen, 2008; Kelemen & Hirth, 2012; Lyer et al., 2008; Plümper et al., 2012; Røyne et al., 2008; Zheng et al., 2018). All these studies demonstrate the impact of fracture development on the reaction rate. A sketch of the fracturing associated with a hydration reaction process is presented in Figure 1b.

Martin and Fyfe (1970) suggested that the rate of serpentinization is rapid over geological times and that it is controlled by the rate at which water is supplied to the reaction surfaces. As the permeability of peridotite is low, and the forming serpentine tends to reduce the porosity of the rock, further reaction should thus depend on the penetration of water through serpentinite into the anhydrous phases of the host rock. Fluid pathways should then be generated during serpentinization in order to expose new reactive surface. However, even if low permeability prevents the complete hydration of the rock, the reaction is not always self-limiting due to reaction-induced fracturing (Figure 1b). Fracturing accelerates the reaction process (Røyne et al., 2008) by providing new pathways for fluids. Recent experimental studies on hydration reactions of periclase or olivine have actually confirmed that reaction-induced fracturing can increase porosity (Zheng et al., 2018; Zhu et al., 2016). The creation of these pathways may be driven by tensile and shear stresses generated from the growth and transformation of a metastable amorphous protoserpentine phase, where stress is localized within surface perturbations (etch pits) and possibly existing cracks (Plümper et al., 2012). In fact, petrographic observations suggest that the intensity of fragmentation of the olivine grains during serpentinization is determined by the progress of the hydration reaction, rather than by external or tectonic forces (Lyer et al., 2008; Malvoisin et al., 2012).

2.2. Effects of Effective Stress and Temperature on Reaction Progress

Several factors control the kinetics of serpentinization. The salinity of the fluid, the presence of CO_2, the mineralogy of the reacting rock as well as the initial grain size of olivine all have influence on the serpentinization process (Lafay et al., 2018; Malvoisin et al., 2012; Martin & Fyfe, 1970). In situ stress state can also influence the reaction rate, as well as the generation of reaction-induced fractures. For instance, Zheng et al. (2018) studied the effect of confinement stress on the coupling between the force generated by mineral growth, reaction-induced fracturing, and porosity evolution during the hydration of periclase (MgO) into brucite ($Mg(OH)_2$). The detailed experimental setup is described in section 4.1. Their analyses showed that reaction-induced fracturing slowed down considerably when the effective mean stress exceeded a threshold of 30 MPa. Below 30 MPa effective mean stress, the fraction of periclase replaced by brucite was a sigmoidal function of time. After a slow initiation, the replacement rate increased with concomitant intense fracturing. The porosity increase resulting from the reaction-induced fractures was transient, that is, pulse-like (Zheng et al., 2018). Following this porosity pulse, the rate of replacement decreased until the replacement was almost complete. Conversely, above 30 MPa effective stress, the reaction rate was slow, and porosity

decreased monotonically without any observable fracturing over the duration of the experiment. Zheng et al. (2018) suggested that the confining pressure generated by the reaction may have overcome the disjoining pressure at the grain-grain interface, expelling the water film trapped there and thereby dramatically reducing the reaction rate. Skarbek et al. (2018) indicated that reaction-induced stresses could be limited by a viscoplastic behavior of the porous aggregate. For example, during the hydration of basanite, the material starts to compact and the creep of the solid matrix may lead to a reduction of the reaction rate. Wolterbeek et al. (2017) performed uniaxial compaction/expansion experiments and measured the force of crystallization generated during CaO hydration. Their results showed crystallization-induced stresses reaching up to 153 MPa, with the reaction stopping or slowing down before completion. They argued that failure to reach up the GPa stresses predicted by thermodynamics theory was attributed to a competition between the increase of the force of crystallization and its inhibiting effect on reaction progress. Their microstructural observations indicated that reaction-induced stresses shut down pathways for water into the sample, hampering ongoing reaction and limiting the magnitude of stress buildup to the values they observed.

The effect of temperature on serpentinization kinetics was first studied by Martin and Fyfe (1970) who demonstrated that the serpentinization rate and temperature relationship (Figure 1c) is maximized at 260 °C. This rate decreased for temperatures below or above this optimum temperature. This was described by Martin and Fyfe (1970) as a symmetric bell-shaped curve. Similar results were obtained by Wegner and Ernst (1983), with a maximum reaction rate value at a temperature close to 310 °C. This discrepancy in the optimum reaction temperature observed among different experimental data sets, which has been observed in other experiments concerned with serpentinization (section 3.3), might be due to differences in the grain size or in the composition of the reactive material used, to the different pressure conditions in which the experiments were performed, or to any other parameters related to the experimental procedure (Malvoisin et al., 2012).

An Arrhenius-type formulation has been proposed to describe the kinetics and the progress of serpentinization and was validated based on experiments performed either with synthetic olivine or pyroxene (Martin & Fyfe, 1970; Wegner & Ernst, 1983). However, these experiments did not integrate the coupled effects of these two coexisting minerals during the alteration of a natural peridotite (Marcaillou, 2011). The Arrhenius formulation has been modified in order to describe the mechanisms involved in a metamorphic reaction, such as serpentinization, which include both surface kinetics and diffusion processes (Lasaga, 1986) in the form of the following expression:

$$f = A.e^{-\frac{E}{RT}}.\left(1-e^{-\frac{m\,\Delta G}{R}\left(\frac{1}{T}-\frac{1}{T_0}\right)}\right) = A.e^{-\frac{b}{T}}.\left(1-e^{-d\left(\frac{1}{T}-\frac{1}{T_0}\right)}\right) \quad (2)$$

where f is a kinetics rate parameter, T is the temperature, A is a preexponential factor of the reaction, E is the activation energy of the reaction specific to each mineral, R is the gas constant, ΔG is the free energy difference of the reaction, m is a constant of the order of unity, and T_0 is a reference temperature. The term T_0 used in this equation is necessary to produce a bell-shaped reaction rate law. This function, derived from the Transition State Theory (Lasaga, 1981, 1995), was also used in Malvoisin et al. (2012). All these parameters have a physical origin and their values depend on the mineralogy of the reactant rock, the stoichiometry of the chemical reactions, and the in situ thermodynamic conditions. Two parameters, b and d, are introduced here to simplify the expression, with $b = \frac{E}{R}$ and $d = \frac{m\,\Delta G}{R}$.

2.3. Reduction of Stiffness and Strength of Ultramafic Rocks Undergoing Serpentinization

Serpentinization causes a reduction of both the stiffness and the strength of the transforming rock body. Peridotite is a stiff rock with high strength (Table 1), while serpentinite is relatively weaker and less stiff (e.g., Guillot et al., 2015). The mechanical properties of these rocks also depend on the confining pressure and temperature conditions they are subjected to (Escartín et al., 1997). The alteration of elastic properties and strength of rocks undergoing serpentinization has fundamental implications on the mechanical and seismic properties of the lithosphere and has thus to be studied. Typical values of stiffness, uniaxial tensile strength, cohesive shear strength and other mechanical properties of ultramafic rocks are presented in Table 1 (Van Noort et al., 2017).

Table 1
Mechanical Properties of Ultramafic Rocks and Component Minerals From Van Noort et al. (2017)

	Rock/Mineral	E (GPa)	U.T.S (MPa)	C.S (MPa)
Peridotite minerals	Olivine (forsterite)	197-216.7	-	177
	Pyroxene (bronzite)	149-152	-	-
Reactant Rock	Peridotite	134.7-168	49.2–284.6	-
Product Rock	Serpentinite	10.6-80	2.3	90

Note. E = Young's Modulus; U.T.S. = Uniaxial Tensile Strength; C.S. = Cohesive Shear Strength.

3. Discrete Element Method Model Formulation

Discrete element models were used to simulate volumetric expansion coupled to fracturing during the hydration of periclase and peridotite. The simulations were performed with Yade DEM, an extensible open-source framework based on the discrete element method (Kozicki & Donzé, 2008, 2009; Šmilauer et al., 2015). The rock material was modeled as an assembly of spherical discrete elements, also called particles, interacting with each other through specific constitutive laws. Since the properties of the discrete elements can be controlled individually, the volume expansion process was simulated by increasing, in a controlled and systematic manner, the radius of each element depending on selected criteria.

3.1. Contact Laws Between Discrete Particles

In our discrete element models, the rock material is represented as a dense assembly of interacting particles. The global mechanical behavior is controlled by the local constitutive laws defined at the particle contacts. In the classic granular description of the medium, only particles in direct contact can interact. The approach used here was different as we defined an interaction range that enables near neighbor interactions between nonstrictly contacting particles (Scholtès & Donzé, 2013). This nonlocal approach enables to account for the role of grain interlocking on the macroscopic behavior of brittle rock and allows reproducing mechanical properties that are specific to rocks such as high ratios of compressive to tensile strengths and nonlinear failure envelopes.

The interaction range is defined by a coefficient γ_{int} ($\gamma_{\text{int}} \geq 1$) that characterizes the distance over which particles may interact. Bonds were created between discrete elements of radius R_i if their respective interaction distances defined by $\gamma_{\text{int}} R_i$ overlapped before the first time step of the simulation (Figure 2a). This interaction range was then set to its default value ($\gamma_{\text{int}} = 1$) after the initial detection time step, thus new interactions could occur only between strictly contacting discrete elements.

The interaction forces were computed from the constitutive laws proposed by Scholtès and Donzé (2013). The normal force F_n, is given by

$$F_n = k_n \, \Delta D \tag{3}$$

where k_n is the normal stiffness calculated as

$$k_n = 2E_{\text{eq}} \frac{R_a R_b}{(R_a + R_b)} \tag{4}$$

Here, ΔD is the relative displacement between the interacting discrete elements, defined as $\Delta D = D - D_{\text{eq}}$, where D is the distance between the centroids of the interacting elements and D_{eq} is the initial equilibrium distance. E_{eq} is the local equivalent of the Young's modulus and R_a and R_b are the radii of the two particles in contact. In compression, F_n can increase linearly with ΔD. In tension, a maximum acceptable force $F_{\text{n,max}}$ is defined as a function of the interparticle tensile strength, t_p, such that, $F_{\text{n,max}} = -t_p A_{\text{int}}$, where $A_{\text{int}} = \pi(_{\text{min}}(R_a, R_b))^2$ is the interacting surface area between particles a and b. When F_n reaches its maximum value, tensile rupture occurs associated to a mode I crack at the contact location, and the interaction is then deleted from the computational scheme.

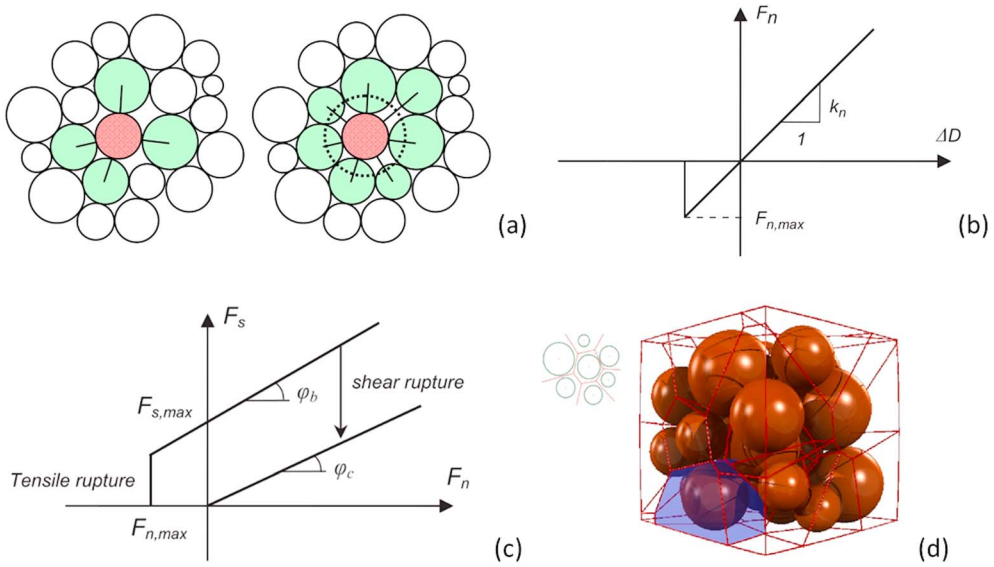

Figure 2. (a) Sketch of the effect of interaction distance on the contact fabric from Scholtès and Donzé (2013). (left) $\gamma_{int} = 1$, (right) $\gamma_{int} > 1$. (b) Normal interaction force between discrete elements and (c) rupture criterion modified from Scholtès and Donzé (2013). (d) Three-dimensional Voronoi diagram that defines the volume cells attributed to each spherical discrete element. Modified from Catalano et al. (2013).

The shear force F_s is computed incrementally by updating its orientation and intensity according to

$$F_s = \left\{F_s\right\}_{\text{updated}} + k_s \Delta u_s \tag{5}$$

with Δu_s the relative incremental tangential displacement and k_s the shear stiffness calculated based on the local stiffness ratio μ and on the normal stiffness k_n such as:

$$k_s = \mu\, k_n \tag{6}$$

Following a Mohr-Coulomb type criterion, the maximum admissible shear force $F_{s,max}$ depends on the normal force, F_n, the cohesion c and the local peak frictional angle φ_b and is calculated as:

$$F_{s,\max} = F_n \tan\varphi_b + cA_{\text{int}} \tag{7}$$

When $F_s \geq F_{s,max}$, a shear rupture occurs associated to a mode II crack at the contact location and the interaction is then deleted from the computational scheme.

If debonded particles come into contact afterward, the normal force follows equations (3) with $F_{n,max} = 0$, and the maximum shear force becomes

$$F_{s,\max} = F_n \tan\varphi_c \tag{8}$$

In the present study, we defined $\varphi_b = \varphi_c$. Although particles have rotational degrees of freedom, no rolling resistance (bending or twisting moments) was considered in this study. This assumption proposed by Scholtès and Donzé (2013), keeps the formulation as simple as possible, without affecting the representativeness of the simulated behaviors.

The discrete element method is based upon an explicit finite difference scheme which is used to solve the dynamic equations governing the motion of each discrete element. In order to keep this scheme stable, the iterative time step was set to be small enough to avoid any numerical oscillations and a local nonviscous-type damping was used to dissipate kinetic energy to ensure each iterative step was close to a quasi-static equilibrium.

In order to characterize the microstructure and the porosity of the simulated medium, we discretized the volume by triangulating over the centers of each particle. In 3-D, each tetrahedron of the resulting mesh comprises a pore volume and a solid volume. Following a procedure called Voronoi tessellation, the dual diagram of this mesh can be computed to identify the reference volumes associated to each discrete element (Figure 2d, Catalano et al., 2013). The local porosity, p_i, associated to a growing discrete element at the simulation time step $t = i$, is calculated as

$$p_i = 1 - \frac{V_{s,i}}{V_{tt,i}} \tag{9}$$

with $V_{s,i}$ the volume of the spherical discrete element and $V_{tt,i}$ the total volume of the Voronoi cell (colored in blue in Figure 2d). In this study, a regular Delaunay triangulation has been used (Chareyre et al., 2011). This is a generalization of the classical Delaunay triangulation to weighted points, where weights account for the radius of spheres. The advantage is that the dual Voronoi graph of the regular triangulation is entirely contained in voids between spheres.

In order to investigate the time evolution of the local porosity change, a relative incremental local porosity R_{inp} is defined as

$$R_{inp} = \frac{p_{i+1} - p_i}{p_{i+1}} \tag{10}$$

where p_{i+1} and p_i are local porosities at two consecutive simulation steps. Therefore, $R_{inp} > 0$ indicates local pore dilation between the two time steps, while $R_{inp} < 0$ indicates local pore size reduction.

3.2. Simulation of Rock Hydration and Volume Expansion

The hydration reaction was modeled, in a first-order approximation, through the volumetric growth of the discrete elements that constitute the initial rock material. The simulations were conducted without fluids. We considered fully drained systems where water can penetrate the rock and hydrate it.

The numerical samples were generated using a DEM calculation following a two-step procedure (Scholtès & Donzé, 2013): first, a cloud of particles was generated by randomly placing noncontacting particles within six rigid frictionless wall boundaries; second, the size of particles was expanded until a predefined isotropic pressure was reached on the boundary walls. The ratio between the normal stiffness and the target pressure was chosen (in the present study, $\frac{k_n}{\text{particle radius} \times \text{isotropic pressure}} = 300$) so as to ensure a limited interpenetration between particles. During the expansion phase, the interparticle friction angle was set to zero, in order to produce a sample as dense as possible. The effect of pore water pressure was taken into account indirectly in the simulations by imposing an effective stress representative of the experimental conditions of Zheng et al. (2018). In order to simulate the process in which the hydration reaction presents a progressive front, the numerical simulation was structured so that the volumetric growth of particles followed a local debonding (equivalent to fracturing) event. The reaction was triggered with one or several particles selected to grow first. These particles may be seen as minerals located in areas where water would preferentially initiate the hydration reaction (e.g., near preexisting pores or fractures). The effect of the number of particles selected to trigger the reaction n_i is shown in the supporting information. The growth of those selected particles induced stress concentration in their vicinity and thus generated interparticle cracking. As soon as an interparticle crack formed, the interacting particles were identified as reacting particles and their respective volume started to increase as well. Their growth caused further fracturing due to stress transfer through their contacts, thus making the reaction front progress within the medium.

The kinetics of the hydration reaction was defined according to an Avrami-type equation (see section 2.1). The amount of expansion was defined as a multiplier applied to the initial particle volume. The volume of a particle V_t at time t was thus defined by

$$V_t = C\left(p_{V\,\exp} + 1\right) V_{ini} = \left(1 - e^{-kt^n}\right)\left(p_{V\,\exp} + 1\right) V_{ini} \tag{11}$$

where C is the extent of transformation described in equation (1), p_{Vexp} is the predefined overall percentage of volume expansion and V_{ini} is the initial volume of the particle. The confinement of the sample was kept

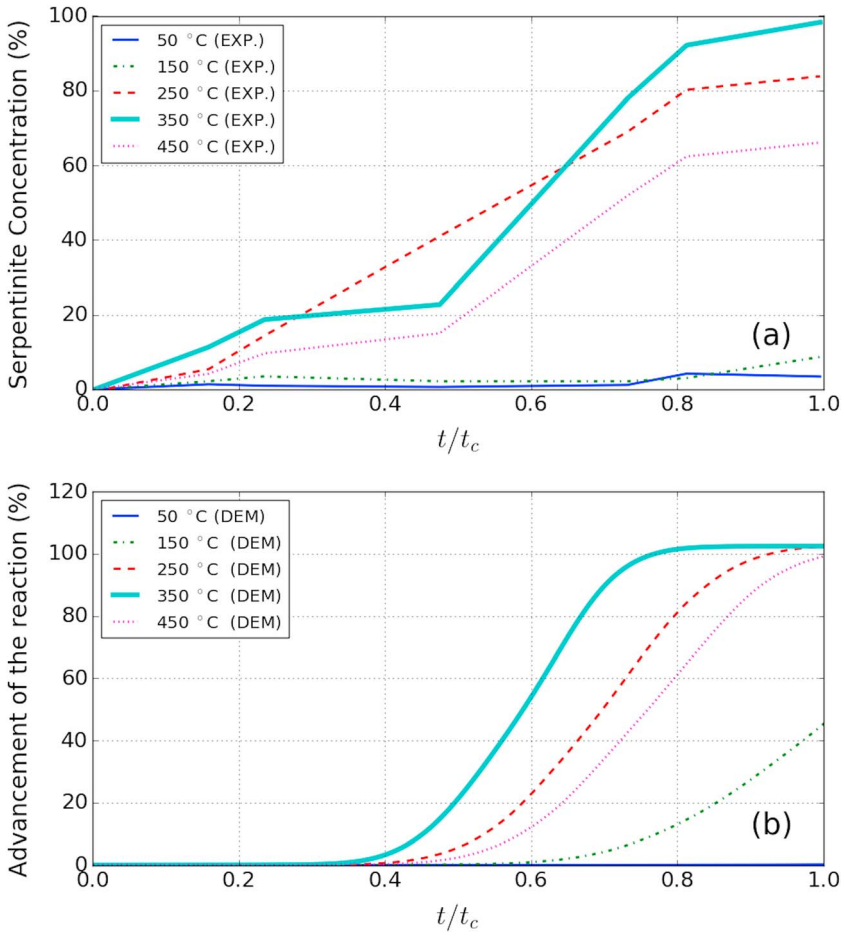

Figure 3. Comparison of reaction advancement versus time for different temperatures in (a) experiments where the advancement was measured by serpentine mass concentration, modified from Marcaillou et al. (2011) and (b) our numerical simulations where the advancement of the reaction was measured by the volume change. On the horizontal axes, t is the time, t_c is the characteristic time used for normalization. t_c = 180 days for experiments, and t_c= 3.77 s for numerical simulations.

constant throughout the simulation. The simulation was terminated once the volume of each solid particles had increased up to the predefined expansion percentage p_{Vexp}.

Since hydration laboratory experiments lasted hours or even days (Figures 3a and 5a), the numerical simulation time needed to be scaled down so as to minimize the duration of the simulations. The explicit time integration scheme used in our discrete element models requires very small time steps of the order of 10^{-8} s to ensure the numerical stability of the simulated system. The critical time step of the scheme should be typically proportional to $\sqrt{\frac{m_p}{k_n}}$, with k_n the stiffness of the contact and m_p the mass of the particle. Considering the experimental time scale in the numerical simulations would thus require infinite number of time steps to complete a simulation and would thus lead to impractical calculation times. To overcome this restriction, we chose to select the values of the two parameters, k and n in equation (11), so as to ensure a quasi-static behavior during the simulations and to keep the ratio numerical time/total duration of numerical time equal to the ratio experimental time/total duration of experimental time for a reference case. The physical parameters (e.g., temperatures, confinement, and stiffness) could be then modified to reproduce other experiments or to do predictive simulations.

3.3. Modeling the Effect of Pressure and Temperature During Serpentinization Reaction

As mentioned previously, it has been observed that the reaction rate decreases under large stress conditions (Skarbek et al., 2018; Wolterbeek et al., 2017; Zheng et al., 2018). Microstructural observations of Wolterbeek

et al. (2017) indicated that reaction-induced stresses shut down pathways for water into the sample, hampering ongoing reaction and limiting the magnitude of stress buildup to the values observed. Skarbek et al. (2018) suggested that the stress limit could correspond to the strength of the material. During compaction, creep can occur, reducing the rate of reaction-induced fracturing. Zheng et al. (2018) indicated that if the stress loading between two grains increases up to the disjoining pressure, the resulting effect is to squeeze out the water film at the contact and further induce the decrease of the reaction rate. In order to account for this effect of stress on the reaction, we modified the Avrami equation by adopting an empirical exponential function related to an empirical parameter γ to slow down the reaction under larger mean effective stress. This empirical parameter γ accounts for various reaction/transport effects, such as the slowdown of the fluid phase transport and the decrease of surface for reaction. The stress control parameter used in the present study was the mean local stress, and we selected a modified Avrami equation with the following form:

$$C = 1-e^{-k\ (t-t_0)^n} = 1-e^{-k_{\mathrm{ref}}\ e^{-\gamma\ \sigma_m}\ (t-t_0)^n} \tag{12}$$

where σ_m is the mean local stress of the particle ($\sigma_m = \frac{\sigma_1+\sigma_2+\sigma_3}{3}$. The local principle stresses, σ_1, σ_2 and σ_3, were computed from the Love-Weber formula (Nicot et al., 2013) and by defining the stress tensor $\overline{\overline{\sigma}}$ associated to each particle i as $\overline{\overline{\sigma}} = \frac{1}{V_{tt,i}} \sum_k \overline{x}^{i,k} \otimes \overline{f}^{i,k}$, with $\overline{x}^{i,k}$ the branch vector linking the particle center to a contact point and $\overline{f}^{i,k}$ the corresponding force), γ is an empirical parameter with unit of Pa^{-1}, t is the time of the simulation, t_0 is the starting time of the growing process of the particle, and n is the scaling time-dependent exponent. In case where $\gamma = 0$, $k = k_{\mathrm{ref}}$, there is no effect of the local mean stress on the reaction rate.

Temperature plays a first-order role on the kinetics of the peridotite to serpentine transformation (Malvoisin et al., 2012; Martin & Fyfe, 1970). We parameterized the effect of the temperature on the rate of advancement by introducing the rate function $f(T)$ in the Avrami equation:

$$C = 1-e^{-f\ (t-t_0)^n} = 1-e^{-A.e^{-\frac{b}{T}}.\left(1-e^{-d\left(\frac{1}{T}-\frac{1}{T_0}\right)}\right)(t-t_0)^n} \tag{13}$$

As a result, the relation that defined the particle volumetric growth at each time step of the discrete element simulations with temperature T as an input parameter became:

$$V_t = \left(1-e^{-A.e^{-\frac{b}{T}}.\left(1-e^{-d\left(\frac{1}{T}-\frac{1}{T_0}\right)}\right)(t-t_0)^n}\right)\left(p_{V\exp}+1\right)V_{\mathrm{ini}} \tag{14}$$

To conduct serpentinization simulations, the values of the four parameters, namely A,b,d,and T_0, need to be estimated, based on experimental observations. Below, we determine the values of these parameters by fitting experimental data from four different studies (Malvoisin et al., 2012; Marcaillou et al., 2011; Martin & Fyfe, 1970; Wegner & Ernst, 1983).

Martin and Fyfe (1970) performed experiments aiming to determine the reaction rate of serpentinization by hydrating synthetic forsterite. They proposed the temperature-reaction rate relationship shown on Figure 1c. Wegner and Ernst (1983) performed a range of experiments on synthetic minerals, from synthetic forsterite to serpentine, in order to characterize the effects of temperature, pressure, and grain size of the reactant mineral on both the hydration and the dehydration reaction rates. The empirical relationships between reaction rate and temperature were qualitatively similar to those obtained by Martin and Fyfe (1970). However, the maximum value of the reaction rate was shifted by 50 °C (Figure 4a). Marcaillou et al. (2011) performed experiments on fresh peridotite xenoliths made up of 65 vol.% olivine, 30 vol.% pyroxene, and 5 vol.% spinel. The concentration in each mineral was monitored during the reaction. The evolution of the reaction of serpentinization was sigmoidal, as shown in Figure 3a. The reaction was very slow at 50 °C, where olivine was stable (Marcaillou et al., 2011). For temperatures between 150 and 350 °C, the reaction accelerated. At 350 °C, the reaction rate maximized and for temperatures above 450 °C, it slowed down. Finally, Malvoisin et al. (2012) studied the kinetics of serpentinization reaction

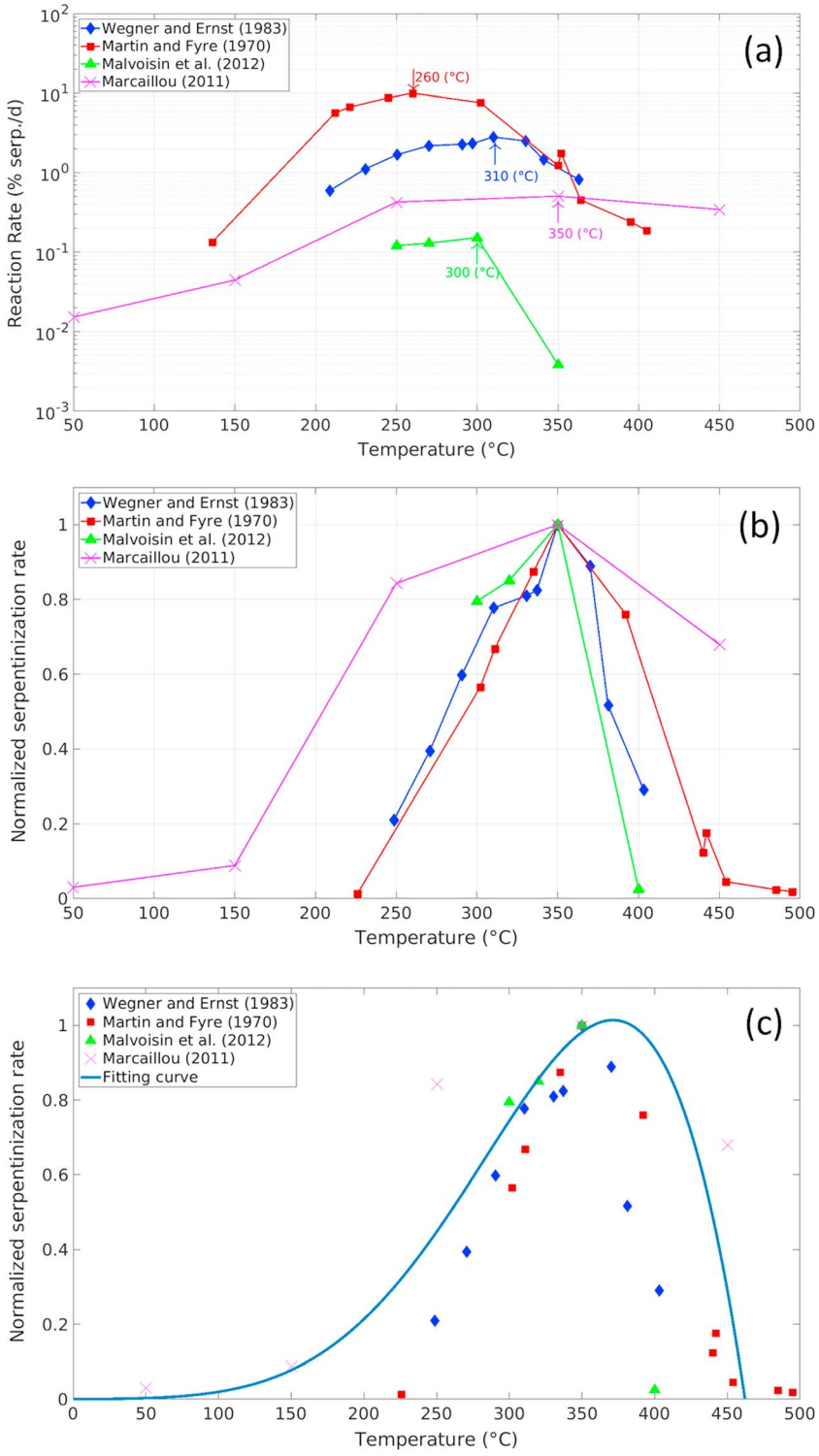

Figure 4. (a) Relationships between the serpentinization rate and temperature from experimental data in four studies. The temperature corresponding to the peak value of reaction rate in each case is indicated. (b) Experimental data after rescaling of the rate axis and horizontal translation of the curves. (c) Fit of the serpentinization rate as a function of temperature, based on four experimental studies.

Table 2
Experimental Conditions in the Four Studies Used to Estimate Kinetics of Serpentine Formation

Reference	Reactant materials	Quantity	Vessel	Grain size	Water/ Rock ratio	Temperature range	T accuracy	Pressure	Pressure accuracy	Duration
Martin and Fyfe (1970)	Synthetic forsterite	60 mg	Sealed Au capsules	58–79 μm	1/4 to 1/ 4.5	130–405 °C	±3 °C	137.9 MPa (20.000 psi)	±2.41 MPa (±350 psi)	6–8 days
Wegner and Ernst (1983)	Synthetic forsterite	80–100 mg	Sealed Ag capsules	37–62 μm	5	208–363 °C	±5 °C	99.6–100.5 MPa	±5%	2–42 days
Marcaillou (2011)	Natural peridotite	25 mg	Sealed Au capsules	~ 1 μm	1	50–450 °C	±6 °C	30 MPa	±1 MPa	190 days
Malvoisin et al. (2012)	Natural olivine	N/A	sealed Au capsules	38–50 μm	2/5	250–350 °C	N/A	50 MPa	N/A	107.5–512.5 days

with respect to temperature, microstructure and grain size. The specific conditions of each experimental study are listed in Table 2.

In all cases, the extent of the reaction was monitored by weighting the mineral assemblage. The weight evolution associated to hydration can be related to the stoichiometry of the reactions (Marcaillou et al., 2011) to obtain the percentage of the conversion. All the data used in the present study are plotted on Figure 4a. The reaction rate, in mass percentage of serpentine produced per day, is related to the reaction kinetics according to

$$Rate = \frac{\text{Percentage of conversion}}{\text{Duration of the experiment}} \tag{15}$$

The differences between the results of these four experimental studies might be due to the different experimental setups and/or the material used. Parameters that are considered to influence reaction kinetics the most are the water to rock ratio and the grain size (Kelemen & Hirth, 2012; Martin & Fyfe, 1970). In all cases, the reaction rates show a maximum value for temperatures between 270 and 350 °C (Figure 4a).

In order to produce a master curve to characterize the temperature effect on the reaction kinetics, a normalization procedure has been applied to the four experimental data sets (Figure 4b). First, the reaction rate of each experimental data was normalized with respect to its maximum value. Second, all the curves were shifted in temperature to coincide with the peak of the curve obtained by Marcaillou et al. (2011). This specific data set was chosen because experiments were performed on natural peridotite and it is the only data set where the evolution of the mineralogy was monitored during the reaction.

The normalized data were fitted using a nonlinear least squares method (Figure 4c). The parameters defining the dependence of the serpentinization kinetics (rate) on temperature (equation (2)) obtained from the fitting process were $A = 79{,}680$, $b = 4{,}745$, $d = 70.56$, $T_0 = 739.3\ K$. With the reference temperature $T_0 = 739.3$ K, the function f meets the following requirements: $T < T_0,\ f > 0$; $T = T_0, f = 0$; $T > T_0,\ f < 0$. T_0 represents the temperature at which reaction product (such as brucite) may become thermally unstable and no longer forms (Zheng et al., 2018). Note that the reaction rate fitted by these parameters not only considers the influence of the temperature, but it also scales the time of all experiments (Figure 4b) with a reference that we use to scale the time of the numerical simulations.

3.4. Modeling the Reduction of Stiffness and Strength of the Transforming Rock

In the discrete element method, the macroscopic mechanical properties of the simulated material emerge from the local parameters defined at the particle scale (section 3.1). To simulate the gradual weakening of the rock induced by the reaction, these local parameters have to be modified during the simulation (Lobo-Guerrero & Vallejo, 2006).

To account for material weakening in our discrete models, the mechanical properties, X', of each particle that had started reacting were modified proportionally to the amount of reaction. Here, X' represents the mechanical properties of a reacted particle such as the local equivalent Young's modulus, E'_{eq}, the tensile

strength, t_p', or the cohesion, c'. X' was calculated by linear interpolation between its initial value X_{ini}, at the onset of reaction, and its final value X_{end}, when reaction was complete, using the particle's advancement of reaction C as a proportionality parameter, as described in equation (16). X_{ini} and X_{end} are input parameters of the simulation.

$$X' = X_{\text{ini}} - C(X_{\text{ini}} - X_{\text{end}}) \text{ with } \begin{cases} X' = E'_{\text{eq}} \Longrightarrow k'_n = 2E'_{\text{eq}} \dfrac{R_a R_b}{(R_a + R_{b)}} \\ k'_s = \mu\, k'_n \\ X' = t_p{}' \Longrightarrow F'_{n,\max} = -t_p{}' A_{\text{int}} \\ X' = c' \Longrightarrow F'_{s,\max} = F_n \tan\varphi_b + c' A_{\text{int}} \end{cases} \tag{16}$$

Similar to equations (4) and (6), the normal and shear interaction forces should be calculated using the reduced local stiffness parameters k'_n and k'_s. These two latter quantities depend on the reduced local equivalent Young's modulus of the material E'_{eq} as well as on the initial radius of the two particles R_a and R_b. Therefore, the reaction implied a modification of several parameters at each time step, including E_{eq}, k_n and k_s, following equation (16). In the same way, for the existing interactions, the maximum acceptable normal force $F'_{n,\max}$ and shear force $F'_{s,\max}$ were calculated with the reduced parameters t' and c' to account for the decrease in strength between the reactant and the product minerals.

4. Results

4.1. Hydration of Periclase into Brucite Under In Situ Crustal Conditions

We model the experimental results obtained by Zheng et al. (2018) to validate our numerical approach. Cylindrical samples of periclase (MgO) ceramics with well-connected initial porosities (0.5–1.6%) and with a diameter of 5 mm and a height of 10 mm were used. Each sample was placed in a triaxial deformation apparatus, where the confining pressure, axial stress, pore fluid pressure, and temperature were controlled independently. A small fluid pressure gradient of 0.5 MPa was imposed between the pore fluid inlet and outlet of the sample to drive fluid flow. The axial and confining pressures were imposed first, then the sample was heated at a rate of 2 °C/min to the desired temperature. Then, the pore fluid pressure was increased to the desired value. The transformation of periclase into brucite was imaged using dynamic X-ray microtomography. The tomograms were segmented to provide estimates of the volume of periclase and brucite throughout the experiments. The experimental conditions for two reference tests, peri1 and peri4, selected over the seven experiments performed by Zheng et al. (2018), are given in Table 3.

During the test Peri1 with a mean effective stress of 5.3 MPa, the percentage of periclase decreased from nearly 98% to 6.8% while the percentage of brucite increased from 2% to 93%, both following a sigmoidal kinetics (Figure 5a). The reaction was almost complete, accompanied with intense fracturing. The overall expansion of the solid volume at the end of the reaction was 110%. Meanwhile, a transient, bell-shaped, porosity pulse with an amplitude of 2% was measured. Conversely, for the test Peri4 run under a higher mean effective stress of 75.3 MPa, the reaction progress was dramatically slower. For the same experiment duration, the replacement of periclase by brucite was very limited and no fracturing could be observed. In the meantime, a decrease of the porosity about 0.7% was measured, which was due to the clogging of initial porosity by the growth of brucite.

Based on these two end-member behavior experiments, completed by five other tests, Zheng et al. (2018) concluded that the effective mean stress has a major influence on the hydration of periclase, regardless the level of differential stresses imposed. When the mean effective stress was smaller than 30 MPa, the reaction was almost complete with extensive reaction-produced fracturing, while when it was larger than 30 MPa, the reaction slowed down significantly and no fracturing was observed over the duration of the experiments (several hours).

We simulated the reaction process presented in Zheng et al. (2018) to better understand how the porosity pulse and the fracture development are related. The size of the numerical sample was 5 mm × 5 mm × 10 mm as in the experiments. The sample contained 1,000 particles of identical size. The radius of each particle was

Table 3
Summary of Experimental Conditions in the Study of Zheng et al. (2018)

Test no.	P_a(MPa)	P_c(MPa)	P_p(MPa)	P_{mean}(MPa)	P_{diff} (MPa)	T(°C)	tc (min)	n_0 (%)
Peri1	11	10	5	5.3	1	210	120	0.53
Peri4	81	80	5	75.3	1	200	180	1.3

Note. P_a = axial stress, P_c = confining pressure, P_p = pore-fluid pressure, $P_{mean} = (P_a + 2P_c)/3 - P_p$ = mean effective pressure, $P_{diff}=P_a - P_c$= differential stress, T = temperature, tc = duration of experiment after temperature was stable and water was injected, n_0= the initial porosity.

0.33 mm. The simulations were conducted under triaxial loading conditions, both the mean effective stress and the differential stress were kept constant during their completion, as in Zheng et al. (2018).

Three parameters were included in our modified Avrami kinetics equation (12) and their values were chosen to be $k_{ref} = 50^4$, $n = 4.0$, and $\gamma = 0.02$ Pa^{-1}. k_{ref} was chosen to ensure a quasi-static reaction process. Small unbalanced forces were measured during the simulation, indicating that inertial effects were restrained. By conducting parametric studies, we verified that the decrease of k_{ref} had no influence on the numerical results, except for controlling the duration of the reaction. The value of n is related to the nucleation and growth law, and a value of 4 was used (Wegner & Ernst, 1983). The choice of γ ensured a slowdown of the reaction occurred for mean effective stresses larger than 30 MPa, meanwhile keeping a reasonable and practical simulation time. The obtained value of γ = 0.02 Pa^{-1} is relatively larger than the equivalent stress dependency factor derived from thermodynamic models, which is estimated in the order of 10–8 Pa^{-1} for hydration of periclase (Kelemen & Hirth, 2012; Wolterbeek et al., 2017). This result confirms that the hydration reaction is likely halted not only by stress effect but by fluid transport effects.

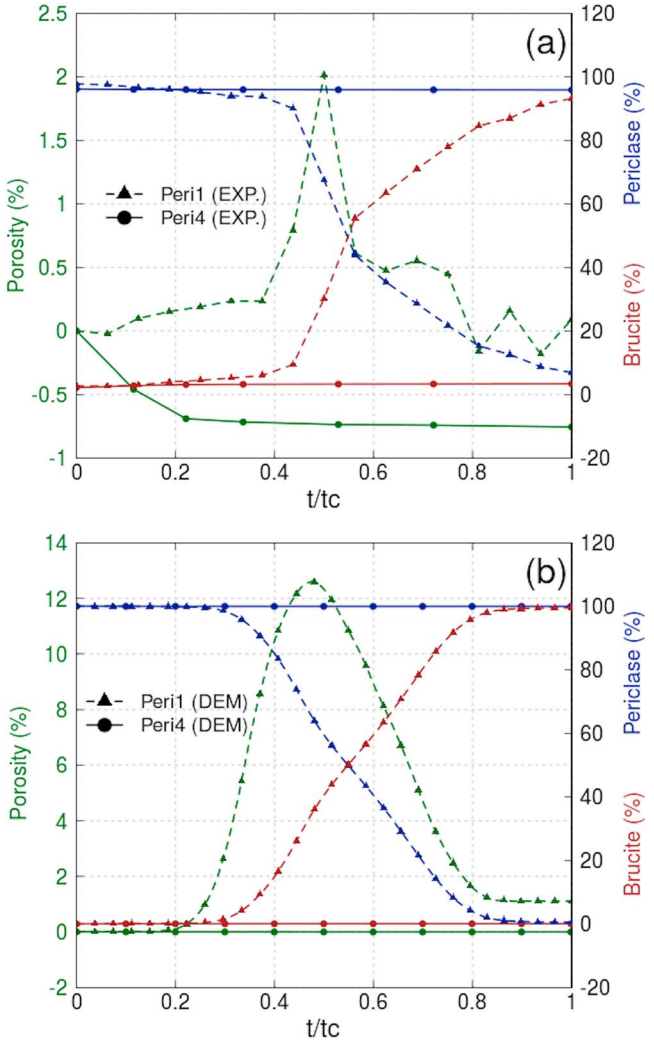

Figure 5. (a) Experimental data for the hydration of periclase into brucite at 180 °C for samples Peri1 and Peri4 described in Zheng et al. (2018). The experimental time t is normalized by the total duration tc (tc = 2 hr for Peri1 and tc = 2.5 hr for Peri4). (b) Numerical data from simulations conducted under similar conditions as experiments (tc =120 ms for Peri1 and tc = 460 ms for Peri4). For both simulations, we consider the case of a propagation of a reaction front (see Figure 6).

In the simulations, the effect of the pore water pressure was indirectly taken into account by imposing the same effective stress values as in the experiments. Thus, to reproduce boundary conditions similar to the test Peri1 in Zheng et al. (2018), the imposed axial confining pressure was 6 MPa, while the horizontal confining pressure was 5 MPa, yielding a mean effective stress of 5.3 MPa. The local constitutive law parameters (Table 4) were determined through a calibration procedure based on a set of uniaxial tension tests and triaxial compression tests (Scholtès & Donzé, 2013), which were used to fit the behavior of the numerical medium to the macroscopic behavior of the periclase (MgO ceramics) used in the experiments (Table 5). Particularly, the calibration of γ_{int} was carried out to ensure a representative ratio between the macroscopic tensile strength and the macroscopic compressive strength.

Two different configurations were considered for the reaction simulation in order to test different modes of reaction initiation. In the first configuration, case (I), a hydration front propagated into the sample from the bottom of the sample. In the second configuration, case (II), the reaction occurred pervasively throughout the sample, initiated from the same number of particles as in configuration (I). These particles were located randomly in the volume. Therefore, case (I) was designed to simulate reaction with a propagation front (fluid infiltration), case (II) was designed to simulate reaction initiation within a homogeneously saturated medium. Case (I) reproduces the conditions for a sample bearing a temperature gradient over a relatively large spatial scale. In this case, the reaction initiates from the bottom boundary where the temperature is higher. Case (II) corresponds to a reaction occurring pervasively

Table 4
Local Interaction Parameters and Physical Property Values Used to Simulate Periclase and Peridotite

Local parameter	Value used for simulating periclase	Value used for simulating peridotite
Interaction range γ_{int}	1.22	1.245
Equivalent Young's modulus E (GPa)	422	200
Local stiffness ratio	0.355	0.2
Local friction angle (particles)	18	18
Friction angle (wall boundaries)	18	18
Tensile strength (MPa)	165	40
Cohesion (MPa)	1,650	400
Density (kg/m^3)	3,580	3,951

throughout the sample. Case (II) reproduces a reaction at the laboratory scale in a sample subjected to homogeneous temperatures. The target of volume increase for each particle was 110% of their initial volume, which corresponds to the volume increase measured experimentally when periclase was hydrated into brucite.

Three-dimensional rendering of the volumetric growth, fracturing, and porosity change inside the simulated sample is shown in Figure 6 for case (I). The pictures describe the sample at five different time steps of the simulation corresponding, respectively, to (1) 0.03, (2) 1.06, (3) 33.5, (4) 70.8, and (5) 99.2% of the reaction completion (see Figures 7a–7c). As expected, the volume of the numerical sample increased during the simulation as the reaction front progressed from the bottom to the top of the sample.

In Figure 6b, the cracks that have formed during the reaction are shown in yellow. The particle growth induced extra stress within the sample that caused the mean effective stress to increase drastically before any significant volume changes could be observed within the sample (Figure 6a). Stress concentrations in the vicinity of the reacting particles triggered interparticle bond breakages (cracking) before the particles had expanded significantly. The local porosity thus only slightly increased in the freshly cracked areas (Figure 6b). As a matter of fact, the propagation of the cracks occurred before the volumetric expansion. The time evolution of the relative incremental local porosity R_{inp} (Figure 6c) showed that, below 33% reaction completion (time step 3), R_{inp} was mainly positive. This indicates that, away from a distinctive propagating front, the pores were predominantly dilating, hence, corresponding to a global increase of the macroscopic porosity. At 33% reaction completion, the global porosity of the sample reached a maximum value and the cracks progressed toward the upper boundary of the sample. In the vicinity of the reaction front, the volume expansion of particles induced pore compression, while other places of the sample showed pore dilation. Above 70% reaction completion (time step 5), R_{inp} was mainly negative, indicating that pores were generally contracting because of clogging, hence, corresponding to the decrease of the macroscopic porosity. The reaction front can be clearly identified based on the distribution of R_{inp} from the bottom to the top of the sample. These results demonstrate that the increase of the macroscopic porosity is due to cracking and pore expansion, while the decrease of the macroscopic porosity after the peak is due to pore clogging.

The time evolution of the advancement of the reaction, the cumulative number of cracks as well as of the increase of global porosity for cases (I) and (II) are presented in Figures 7a–7c. The simulation time was normalized by the characteristic time, *tc*, which corresponds to 99% completion of the reaction. The model simulated a relative porosity evolution from an initial state.

Table 5
Mechanical and Physical Properties Used for Periclase (Magnesium Oxide Ceramics), From Spriggs et al. (1962) and Chung et al. (1963)

Property	Value
Mechanical properties	
Young's modulus	306 GPa
Poisson's ratio	0.172
Density	3,580 kg/m^3
Physical properties	
Compressive strength	1,660 MPa
Tensile strength	160 MPa

As shown in Figures 7a–7c for case (I), the advancement of reaction, calculated as the percentage of global reaction completion, presented a sigmoidal evolution over time. This is an expected result, since the expansion of particle volume was controlled by an Avrami type reaction. A similar evolution was observed for the cumulative number of cracks. Conversely, the incremental global porosity showed a pulse-like evolution with a maximum value of 12%. This pulse is in agreement with the observations made by Zheng et al. (2018) even though its value is larger (2% in the experiment). For case (II), the advancement of the reaction, the

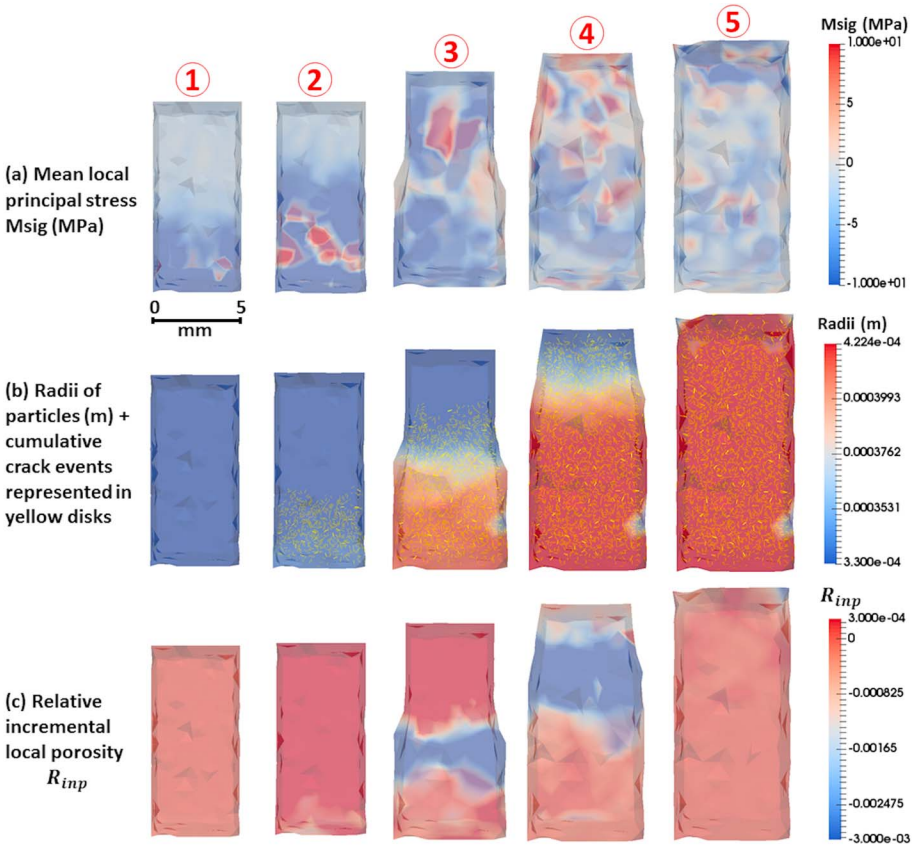

Figure 6. Model configuration with the propagation of a reaction front at five time steps labeled 1 to 5, corresponding to 0.03%, 1.06%, 33.5%, 70.8%, and 99.2% reaction completion, respectively (see also Figures 7a–7c). Case (I). The expansion occurs along a front that propagates in the sample. View of (a) the mean local principal stress Msig, (b) the radii of particles as well as the cumulative crack events presented in yellow disks, (c) the relative incremental local porosity R_{inp}.

cumulative number of cracks, and the increase of global porosity showed comparable trends to case (I). The porosity pulse had an amplitude of 7%, which is closer to the experimental value measured by Zheng et al. (2018). Both reactions lasted approximately the same duration. The cumulative number of cracks in the two cases was similar, but it took longer time for the sample to experience intense cracking in case (II). The deformation induced by the first particles' expansion was less concentrated in case (II), causing cracking to occur later on during the reaction. The peak of the porosity pulse occurred at approximately 30–35% of reaction completion for both cases. The sigmoidal shape of the advancement of reaction, the fracturing, and the porosity pulse observed in the experiments of Zheng et al. (2018) were reproduced in both numerical simulations. However, the porosity pulse amplitudes obtained in both cases are larger than the value measured by Zheng et al. (2018). Possible reasons for this difference are discussed in section 5.1.

To further compare cases (I) and (II), two parameters were defined. The first parameter was the rate of fracture development, which was defined as the steepest slope of the cracking curve at the time corresponding to the peak value of porosity pulse (Figure 7b). The second parameter, t_{ndp}, was defined as the time duration of the porosity pulse within 50% of its peak value (Figure 7c). Both parameters had been normalized by their maximum value. Results indicate that case (II) is associated to a relatively larger rate of fracture development but, at the same time, with a relatively lower porosity pulse and a smaller value of t_{ndp}.

To characterize the variability of the results when the initial particle microstructure is varied, we performed simulations using three different initial packings. The three samples contained 1,000 particles with the same uniform grain size distributions, where the maximum particle size was twice larger than the minimum particle size. The difference between each packing stands in the generating process, which distributes randomly the particles within the volume to fill. The time evolution of the advancement of reaction, the cumulative number of cracks, and the increase of global porosity for simulations performed with the

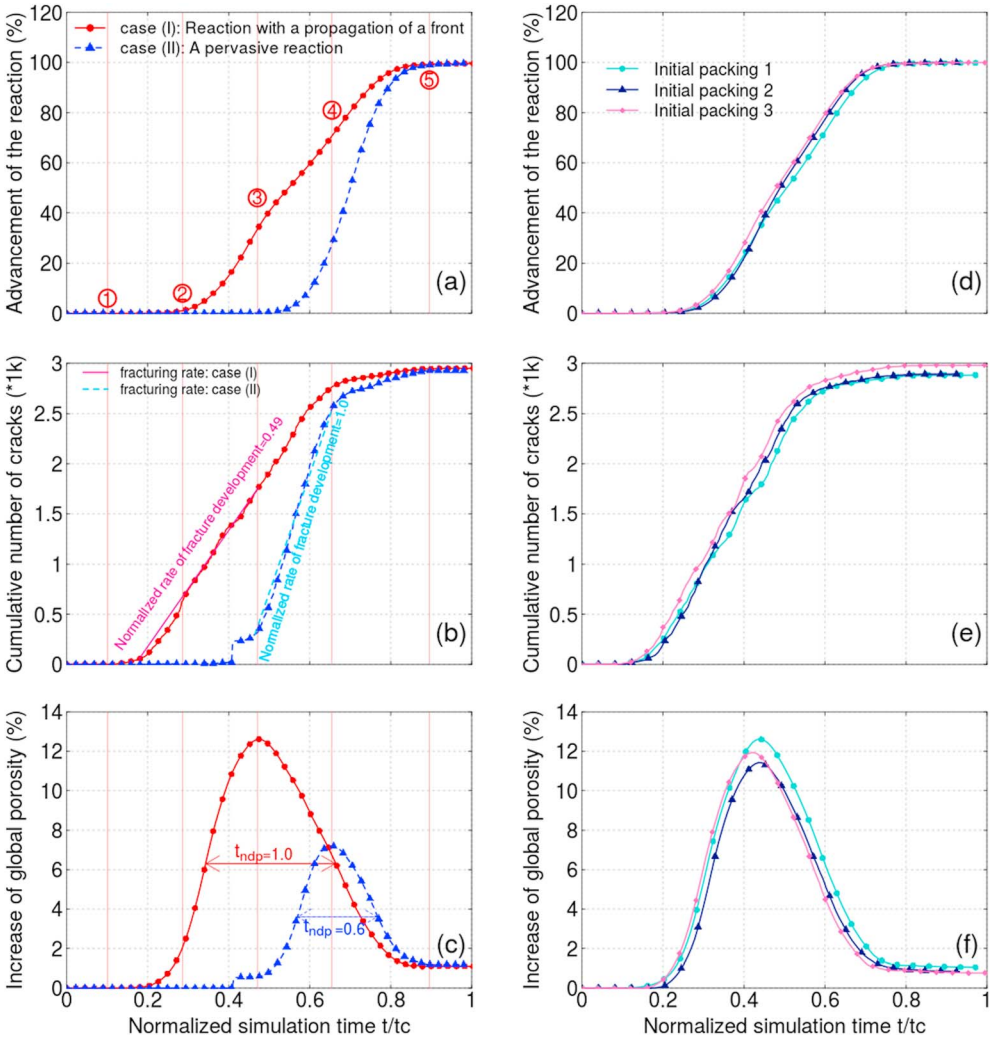

Figure 7. Simulation of periclase hydration for the cases of propagation with a (I) reaction front and (II) pervasive reaction. (a–c) Time evolution of (a) the advancement of reaction (time steps labeled 1 to 5 are shown in Figure 6), (b) the cumulative number of cracks, (c) global porosity of the sample during volume increase, where t_{ndp} is the time duration of the porosity pulse within 50% of its peak value. (d–f) Time evolution of (d) the advancement of reaction, (e) cumulative number of cracks, and (f) incremental global porosity for three simulations where the discrete elements had a polydisperse-size distribution, for the case (I) of propagation with a reaction front.

propagation of a reaction front (case (I)) are presented in Figures 7d–7f. The simulation time was normalized regarding to the reference time *tc* (*tc* =120 ms). The results obtained for these three different initial packings were very similar and followed the same trend as the ones presented in Figures 7a–7c. The standard deviation of the peak value of porosity pulse was less than 2%, which confirms therefore the reproducibility of the results. In addition, the small variability of the results obtained with different initial microstructures confirms that the samples used in the present study were large enough to be considered as REV (representative elementary volume).

The distributions of the first invariant of the local stress tensor I_1 and of the square root of the second invariant of the local deviatoric stress tensor $\sqrt{J_2}$ are plotted in Figure 8 at different advancements of the reaction for case (I). I_1 and $\sqrt{J_2}$ were defined as

$$I_1 = \sigma_1 + \sigma_2 + \sigma_3 \tag{17}$$

$$\sqrt{J_2} = \sqrt{\frac{1}{6}\left[(\sigma_1-\sigma_2)^2 + (\sigma_2-\sigma_3)^2 + (\sigma_3-\sigma_1)^2\right]} \tag{18}$$

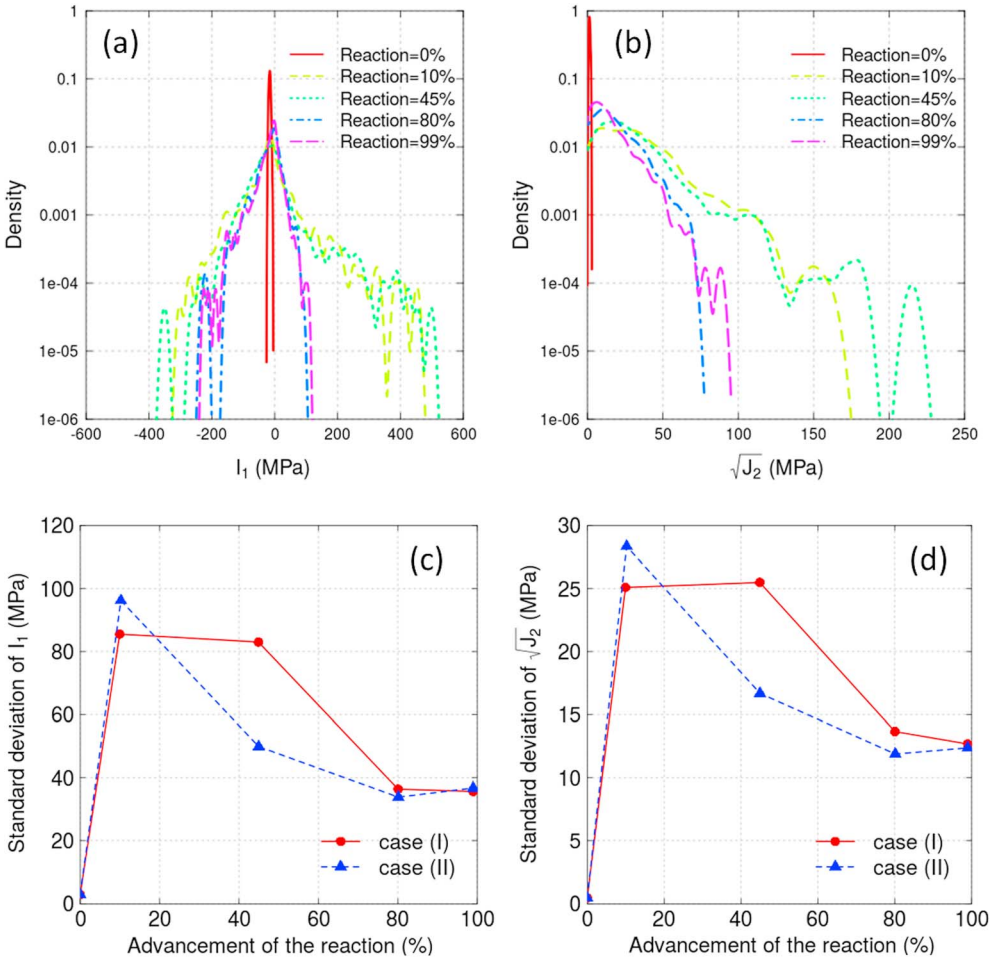

Figure 8. The density distributions of (a) I_1, the first invariant of the local stress tensor, and (b) $\sqrt{J_2}$, the square root of second invariant of the local deviatoric stress tensor, at different advancements of the reaction considering the progression of a reaction front of case (I). The standard deviations of (c) I_1 and (d) $\sqrt{J_2}$ at different advancements of the reaction for simulations of cases (I) and (II).

where σ_1, σ_2,and σ_3 are the local principal stresses of a particle. Thus, I_1 represents only the contribution of the hydrostatic stress, that is, pressure, while $\sqrt{J_2}$ represents the contribution of the shear stresses.

At the onset of the reaction, I_1 shows a nearly Gaussian distribution representative of a small standard deviation (Figure 8a). In this figure, negative values indicate tensile stress. The mean value of I_1 was equal to 16 MPa, which is consistent with the boundary stresses (axial stress of 6 MPa and confining pressure of 5 MPa). For a reaction completion between 10% and 45%, the distribution for both invariants spread across larger stress spectrum. This wider distribution is related to the expansion of particles, which produced large stress variability within the sample. When the advancement of the reaction was larger than 80%, the distribution of I_1 returned to a nearly Gaussian distribution again, but with a larger standard deviation compared to the initial distribution. The standard deviations of I_1 and $\sqrt{J_2}$ at different advancements of reactions for cases (I) and (II) are shown in Figure 8c and 8d, where similar trends can be noted for both cases.

The model was used to simulate another experiment where the average mean stress was larger than 30 MPa and in which no reaction-induced fracturing was observed (sample Peri4, Zheng et al., 2018). Similarly to the simulation of peri1 experiment, we used the modified Avrami relationship presented in equation (12) and adopted $k_{\text{ref}} = 50^4$, $n = 4.0$, and $\gamma = 0.02$ Pa^{-1} to apply an exponential cutoff effect of the mean stress on the reaction rate. The axial stress applied in the simulation was 76 MPa, and the confining pressure was 75 MPa. The results for the simulation performed considering the propagation of a reaction front (case (I)) are presented in Figure 9.

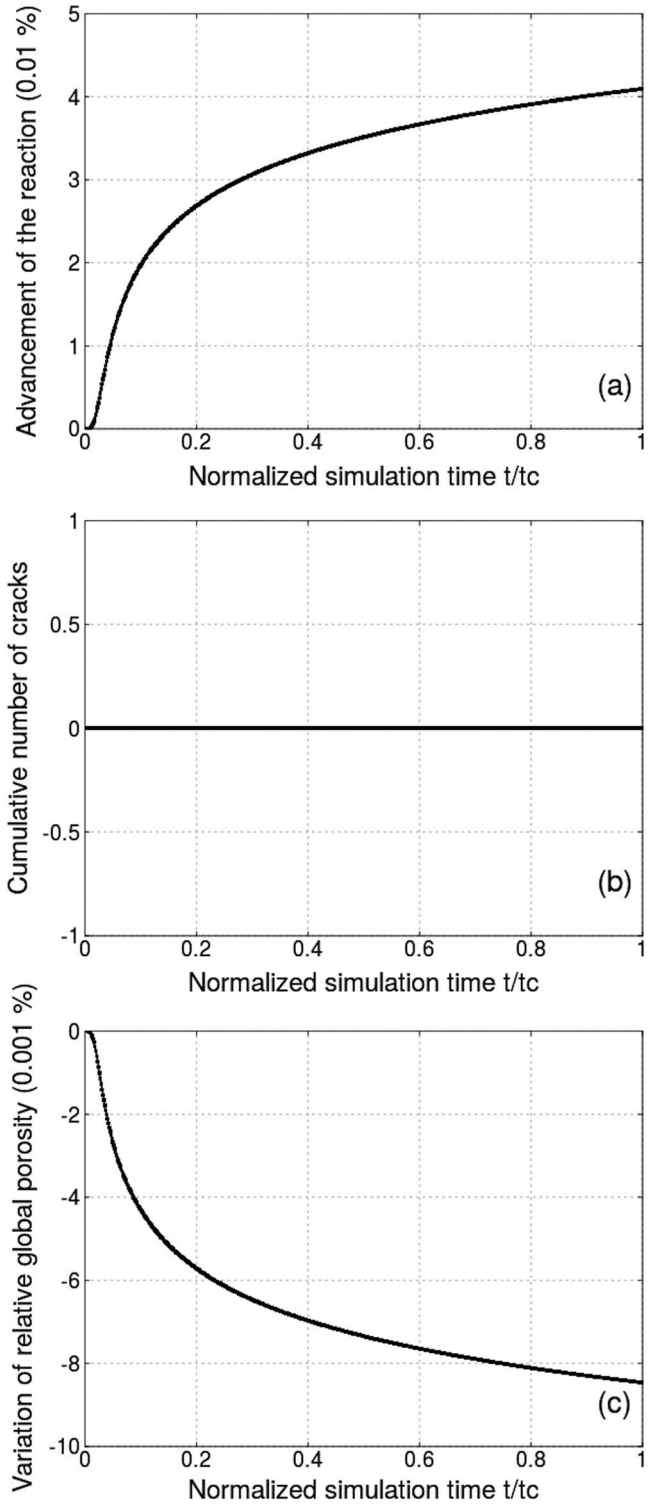

Figure 9. Simulation of the periclase to brucite reaction at 75.3 MPa effective mean stress (sample Peri 4 in Zheng et al., 2018), where the reaction is slowed down. (a) Advancement of the reaction versus numerical time. (b) Cumulative number of cracks. (c) Variation of relative global porosity as a function of time. The numerical time t is normalized by the total duration tc (tc = 460 ms).

Under 75.3 MPa mean effective stress, the reaction progress was very slow. In agreement with the experimental test Peri1, 99.9% of reaction was completed at t/tc = 1.0 in the simulation (Figures 7a–7c). Conversely, only 0.04% of the reaction was completed for the simulation that reproduced the conditions of the Peri4 test. The total duration tc for Peri4 was 3.8 times bigger than tc for Peri1. In addition, no cracks were observed and the global porosity showed a decreasing trend in both experiment and simulation. The decrease in global porosity (0.008%) was smaller than the experimental value (0.7%). This difference is discussed in section 5.1.

Overall, our numerical simulations reproduced many observations made in the experiments performed by Zheng et al. (2018): the sigmoidal kinetics reaction, the process of reaction-induced fracturing for mean effective stress below 30 MPa, the decrease of the reaction rate above this value, and the existence of a transient porosity pulse (Figures 5a and 5b). In light of these results validating our numerical approach to hydration of periclase to brucite, we extended our model to study the serpentinization process.

4.2. Hydration of Peridotite and Effect of Temperature on the Kinetics of Reaction

The numerical sample considered here had dimensions of 1 m × 2 m × 1 m. The size of the sample was chosen here to optimize the simulation time since the simulated behavior of our model is size independent. The sample contained 1,000 monodisperse spherical discrete elements. It was submitted to a triaxial loading in order to reach a predefined isotropic stress state of 30 MPa, a stress value representative of in situ serpentinization reactions (Marcaillou, 2011). The local mechanical properties were adjusted to fit the behavior of the model to the behavior of the peridotite (Van Noort et al., 2017). These parameters are listed in Table 4. To account for the effect of temperature on the rate of reaction-induced volume increase, the formulation presented in equation (14) was considered.

Simulations were conducted at different temperatures (Figure 3b) and the numerical outputs were compared to the experimental data obtained by Marcaillou (2011) who performed five serpentinization experiments at temperatures of 50, 150, 250, 350, and 450 °C. The overall solid volumetric increase prescribed to the model was 30%, a value relevant to the volumetric growth associated to serpentinization processes (Kelemen & Hirth, 2012). The parameter n in equation (14) was set to 5. The comparison between the experimental data and the numerical results is shown in Figure 3.

The reaction rates (Figure 4b) as well as the time scales (Figure 3) were normalized for all experiments to make the end of the hydration process to correspond to t = 1. In Figure 3, both simulation times and experimental reaction times corresponding to the five temperature conditions were normalized regarding to a characteristic time t_c. For the simulation output, t_c was defined as the duration at which the fastest simulated reaction was complete, the latter being the one performed at T = 350 ° C (t_c = 3.77 s). For the experimental data, t_c was taken equal to 180 days because it corresponded to the time for which serpentinization had been completed the fastest, at T = 350 ° C as well. Both vertical axes were also normalized, so that the upper limit (100%)

corresponds to the completion of all particles' growth in the simulations and the transformation of all the available material to serpentine in the laboratory experiments, respectively.

The comparison is made here by following the evolution of two different quantities: the volumetric growth in the numerical simulations and the concentration of serpentine in the experiments. Both quantities are indicators of the advancement of the reaction and both follow the sigmoidal curves related to the physical process. They can thus be used to compare the main manifested trends. The trends related to the temperature effects on the reaction that were observed in the experimental data, were correctly reproduced by the model. For the duration defined within the characteristic time, both in experiments and simulations, the reaction did not even start at low temperature of 50 °C. For temperatures ranging between 150 and 350 °C, the reaction accelerated significantly. At 350 °C, the reaction rate was maximal. For temperatures higher than 450 °C, the rate was again reduced. The simulations were also able to reproduce the bell shape of the temperature—reaction rate curves observed experimentally.

5. Discussion

5.1. Modeling Experimental Periclase Hydration Reactions

The proposed model was able to reproduce several observations made by Zheng et al. (2018) such as the volume increase due to hydration reaction, the sigmoidal shape of the reaction evolution, the formation of fractures, the existence of a transient porosity pulse, and the slow-down effect of stress on the reaction rate (Figure 5). For the hydration of peridotite, the numerical simulations reproduced the bell-shaped temperature-reaction rate relationships observed in serpentinization experiments (Marcaillou et al., 2011).

For the sample confined under lower effective stress (Peri1), the amplitude of the porosity pulse was larger in the simulations than in the experiments. One possible reason for this difference lies in the different boundary conditions used in the experiment and in the numerical simulations (Figure 10). The experimental sample was surrounded by a flexible jacket, while rigid walls were used in the numerical simulations. When the reaction occurred through the progression of a front in case (I), the expansion of particles located near the rigid walls produced pinch points which generated larger stresses on these walls. The walls had then to move backward entirely to maintain the confining pressure constant. This servocontrolled procedure thus generated larger deformations and, hence, larger pore volume variations in the numerical simulations compared to the experiments where the membrane adapted to the morphology of the rock sample. The difference in the porosity pulse amplitudes observed in the numerical simulations of cases (I) and (II) for sample Peri1 gave further support to this hypothesis. For instance, since the reaction initiated from particles randomly distributed in case (II), the expansion of these particles built less pinch points along the sample boundaries, which would then produce less excess stress on the walls and thus less overall volumetric variations. Pore dilation was more distributed over the sample in case (II) compared to case (I). Another reason for this difference might be related to the shape of the particles used in the simulations. Although the use of spherical particles in discrete element method minimizes the computational costs, relatively large porosity pulse amplitudes may be generated in the numerical simulation due to the lack of grain interlocking effect compared to experiments performed on low-porosity rocks. Finally, the simulation did not consider the different mechanical properties of periclase and brucite, whereas the stiffness of brucite is particularly smaller than that of periclase. The effect of changing stiffness during the reaction is quantified in section 5.2 and remains modest.

For samples under higher effective stress (i.e., sample Peri4), the simulation was able to reproduce the decrease of porosity observed in the experiments of Zheng et al. (2018). However, the magnitude of decrease (0.008%) was much smaller in the simulation than in the experiment (0.7%). The difference might be due to the different setups used respectively in the numerical simulations and in the experiments. In the experiments, the decrease of porosity was due to the precipitation of newly generated brucite particles that filled existing pores, while in the numerical simulations, the porosity decrease was only due to the contraction of a limited number of pores associated to slightly reacting particles.

Another common point between experiments and numerical simulations is the distribution of cracks. In the experiments, the induced cracks appeared as vein network or mesh texture (Malvoisin et al., 2017; Plümper

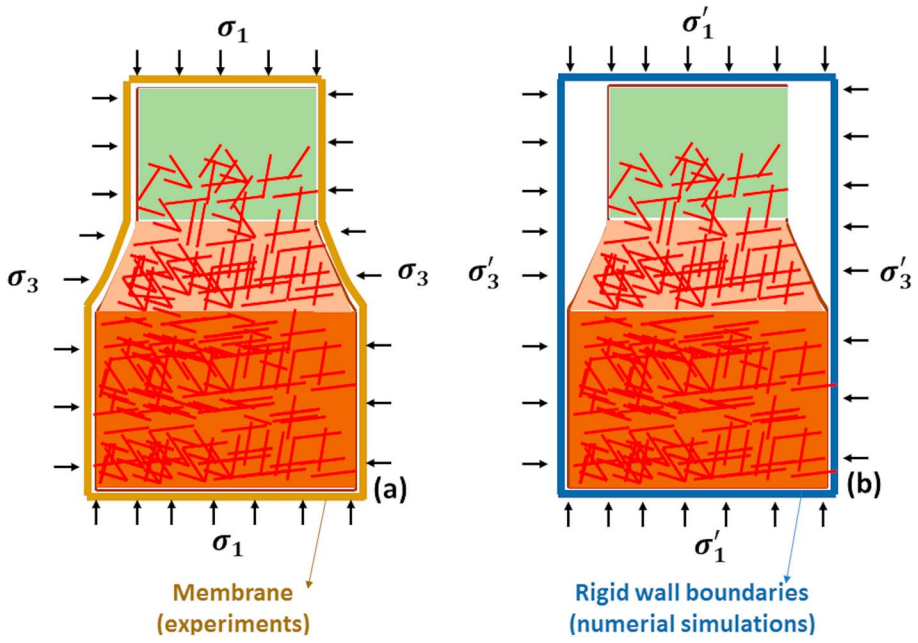

Figure 10. Different boundary conditions in (a) experiments and (b) numerical simulations.

et al., 2014; Zheng et al., 2018). In the numerical simulations, the creation of connected cracks forming similar networks precedes the reaction front (Figure 6b).

We note that two kinds of reactions were considered: either a propagation front (case (I)) or a reaction initiated pervasively within the sample (case (II)). In case (I), the permeability of the zones that had already reacted tends to decrease due to the volume increase, while the permeability of the zones above the reaction front tends to increase due to fracturing. In this case, it is reasonable to consider that the fluid can flow through the sample and hydrate it. In case (II), the reaction initiates pervasively within the sample and induces a decrease of permeability locally within the sample. In this case, some fluid would be trapped locally since the fractures cannot be connected and fluid transport inside the sample would thus be slower. The model needs to be enriched to better characterize this complex fluid transportation, a prospective of this work. Moreover, in the present study, we decoupled the respective contributions of stress and temperature on the reaction rate. One extension of our work would be to set up a formulation which couples stress and temperature effects on the reaction rate. However, experimental data obtained under various temperature and stresses conditions necessary for validating such model are still lacking.

5.2. Transformation of the Mechanical Properties of the Rock During Reaction-Induced Fracturing

The reduction of stiffness and strength associated with serpentinization should have an effect on the fracturing process. According to Van Noort et al. (2017), the Young's modulus of peridotite is 10 times larger, or more, than that of serpentinite, depending on mineralogy and in-situ conditions (Table 1). In the following, we incorporate this weakening effect in the simulations to evaluate its influence on the serpentinization process.

Four different numerical setups (cases 3–6) were considered and compared to each other. Case 3 corresponds to the original model where all the mechanical properties of the medium remained stable throughout the simulation. Case 4 considers a reduction of the interparticle stiffness during the reaction. In case 5, the interparticle tensile strength and cohesion were reduced during the simulation, while the stiffness remained unchanged. Cases 4 and 5 were designed to investigate the influence of the strength reduction separately from the effect of stiffness reduction. Finally, in case 6, all the interparticle parameters (stiffness, tensile strength, and cohesion) were reduced as the reaction progressed. A verification of the code for stiffness reduction based on a scheme with five particles is given in the supporting information.

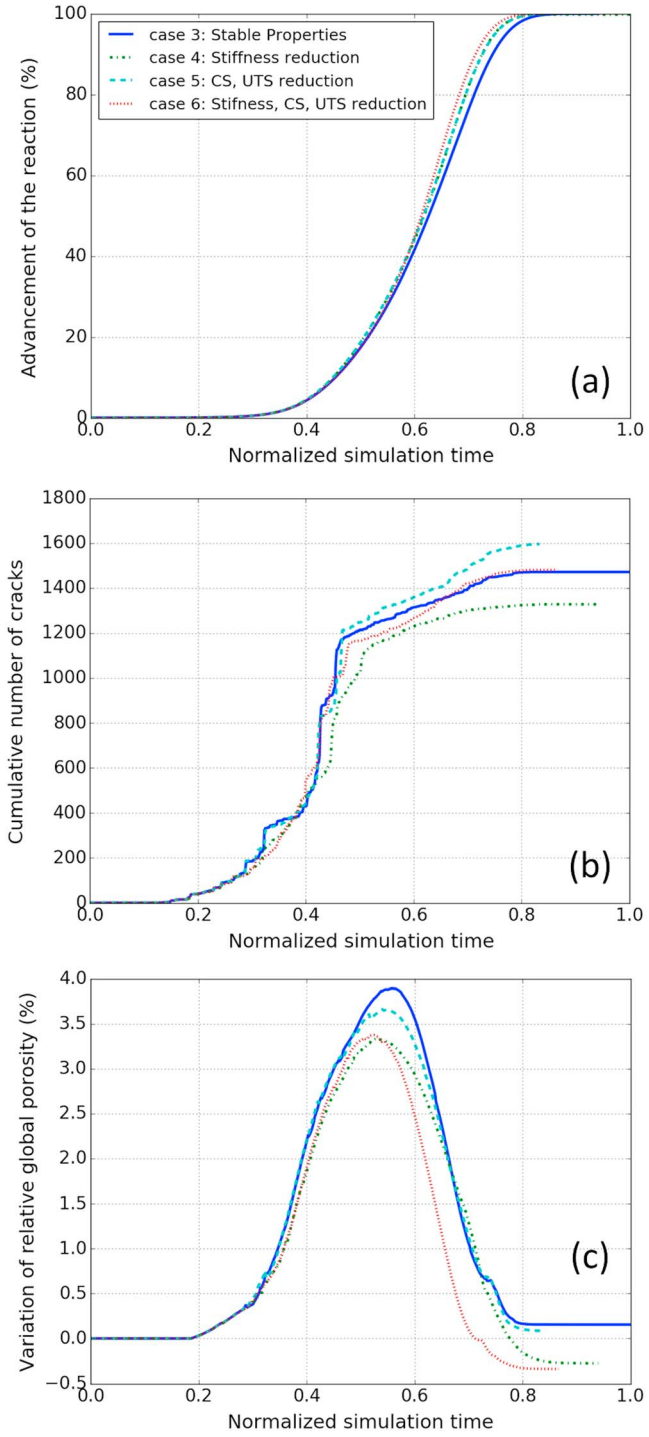

Figure 11. Effects of the evolution of mechanical properties of the rock during serpentinization in four numerical configurations: stable mechanical properties (case 3), stiffness reduction (case 4), strength reduction (case 5), both stiffness and strength reduction (case 6). (a) Advancement of the reaction measured by the volume of the solid phase. (b) Cumulative number of cracks. (c) Variation of relative global porosity. In each case, the simulation time is normalized by t_c,t_c= 3.77 s.

The mechanical properties were modified proportionally to the particle volumetric growth and adjusted at each time step. For all simulations, the sample contained 400 discrete elements, the isotropic confinement was 30 MPa, the temperature was 350 °C and the total volumetric growth was30%. The initial and final microparameters were E_{ini} = 200 GPa, E_{end} = 20 GPa, t_{ini} = 40 MPa, t_{end} = 4 MPa, and c_{ini} = 400 MPa, c_{end} = 40 MPa, respectively.

The duration of the reaction remained unchanged in the four cases. As shown in Figure 11, the reduction of the mechanical properties had a very limited impact on the time of the onset of reaction and on the shape of the Avrami type kinetics. A slight ~10% increase of the serpentinization rate was observed in case 6 when all mechanical parameters were varied (Figure 11a), compared to case 3 where the mechanical properties remained constant. The timing at which the porosity began to increase significantly and the shape of the porosity pulse remained similar for all four configurations. The duration of the porosity pulse remained identical for cases 3–5, which was slightly larger than in case 6 (Figure 11c).

When the stiffness was reduced during the reaction, 10% less cracks formed in case 4 than in case 3 (Figure 11b). The drop of crack number observed between cases 3 and 4 was reproduced in cases 5 and 6. In our discrete element models, the normal interaction forces are calculated from the normal interaction stiffness, as $F_n = k_n \Delta D$. Therefore, when the stiffness is reduced, smaller forces develop and, by consequence, fewer cracks nucleate. The cracking was most prominent in case 5 (Figure 11b). This was expected because the stiffness in this case was not reduced (the contact force should be same as in case 3) while the strength was reduced, hence promoting cracking. These results also provide a verification of the robustness of the model. In every case, the observed differences were small with respect to the amplitude of the overall process.

As shown in Figure 11c, stiffness reduction induced a decrease of the porosity pulse amplitude, which can be observed when comparing case 3 to case 4, and case 5 to case 6. This result might be related to the fact that smaller stiffness results in larger overlapping between particles. Since the interpenetration between discrete elements was larger, the space in between them, representing the pore space, became smaller. This is expected because a softer and more deformable rock would fill-in the fracture induced pore space more easily than a stiffer one. The strength reduction did not influence the amplitude of porosity pulse in our simulations. To conclude, our numerical simulations demonstrate that variations of strength and elastic properties induced by the reaction produce small differences in terms of fracturing and porosity and can thus be considered as a second-order effect in such process.

5.3. Modeling Serpentinization in Natural Conditions

The interplay between fracturing of the rock and induced porosity changes at various temperatures were investigated by tracking the relationship between the peak value of porosity pulse and the normalized rate of fracture development (Figure 12a, see Figure 7b for the definition of the rate of fracture development). The rates of fracture development observed for the five temperatures were normalized by the maximum value among them. Results indicate that, between 50 and 350 °C, the rate of fracture development increased with temperature. It reached a maximum value at 350 °C and decreased at 450 °C. Conversely, the amplitude of the porosity pulse was minimum at 350 °C and increased for temperatures

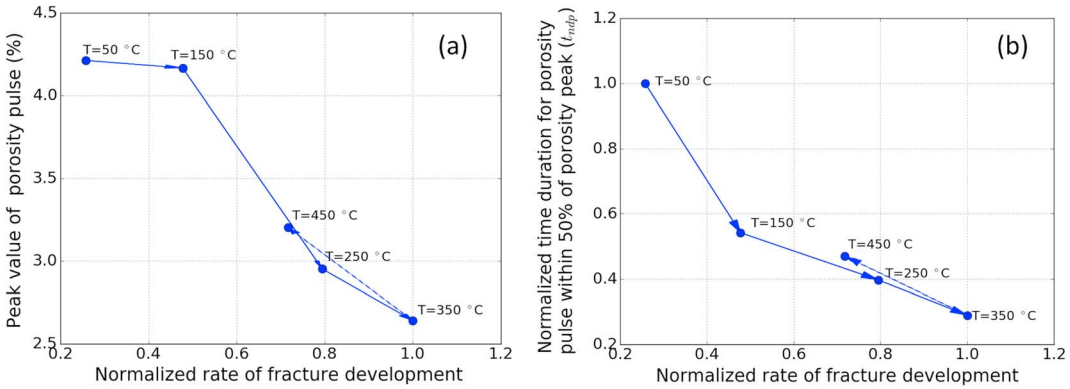

Figure 12. (a) Relationship between peak value of porosity pulse and the normalized rate of fracture development for modeled serpentinization reactions at five different temperatures. (b) Normalized time duration for porosity pulse within 50% of porosity peak as a function of the normalized rate of fracture development.

below or above this optimum temperature (Figure 12a). These results further suggest that a higher fracturing rate is related to a lower amplitude of the porosity pulse. This result is consistent with the trend observed for the hydration simulation of periclase of specimen Peri1 of Zheng et al. (2018) for case (I) and case (II) presented in Figures 7a–7c. Therefore, the optimum temperature associated with the fastest reaction rate did not correspond to the largest porosity value increase. Because large rates of fracture development arise from rapid volume growth, this volume increase tends to clog the poral space faster, and the newly generated porosity has less time to increase.

The relations between the time duration of the porosity pulse t_{ndp} (see Figure 7c for the definition of t_{ndp}) and the rate of fracture development were investigated. The t_{ndp} values corresponding to the five temperatures were normalized by the maximum value among them. From 50 to 350 °C, t_{ndp} decreased with the temperature (Figure 12b). It reached a minimum value at 350 °C and increased at 450 °C. Similarly, higher rate of fracture development was related to lower values of t_{ndp} (Figure 12b).

The studies of Marcaillou et al. (2011) suggested that a temperature of 350 °C provided the maximum reaction rate. This observation is confirmed by our numerical simulations. On the other hand, our numerical results indicated that the amplitude of the porosity pulse and the duration of this porosity pulse at 350 °C were minimum among the five investigated temperatures. Particularly, at other temperatures (50, 150, 250, and 450 °C), the amplitude of the porosity pulse was up to 1.59 times larger, and the duration of the porosity pulse was up to 3.45 times larger. Therefore, our study suggests that additional parameters like kinetics of the reaction, grain size, quantity, and duration of porosity pulse, might play a role in addition to temperature.

The transient porosity pulse observed during hydration reaction is related to fracturing, as observed for the hydration of periclase (Zheng et al., 2018). The increase of porosity is due to fracture opening while the decrease of porosity is due to fracture clogging (Figure 6) as suggested by both the experiments of Zheng et al. (2018) and our numerical simulations. The occurrence of the fractures and the porosity pulse probably change transiently the permeability of the rock and facilitate fluid flow, which would enhance further reactions in a positive feedback loop (Jamtveit, Malthe-Sørenssen, & Kostenko, 2008; Kelemen & Hirth, 2012). The migration of fluids also depends on the amount of porosity increase and on the duration of the porosity pulse. The migration of fluid may be limited when the porosity pulse presents a low amplitude and a short duration. Moreover, the reaction-induced fracturing process induces large stress concentrations within the medium, promoting the transient generation of potentially large shear stresses (Figure 8). These large shear stresses could explain the existence of microseismic activity observed near slow spreading oceanic ridges which was interpreted as resulting from active serpentinization at depth (Horning et al., 2018; Schlindwein & Schmid, 2016).

The modeling of serpentinization proposed in this study provides additional information compared to previous studies (Kelemen & Hirth, 2012; Skarbek et al., 2018). In the present study, serpentinization was

simulated in an explicit way by coupling the chemical reaction to the deformation. The formation of fractures and the associated transient porosity pulse could be reproduced. The investigations took into account not only the effects of temperature on the reaction rate but also the reduction of material properties during the reaction. The coupling between fracturing, porosity changes, and their consequences on permeability have geodynamic implications (Cannat et al., 2010; Malvoisin et al., 2017; McCollom & Bach, 2009; Plümper et al., 2014). For instance, the fact that larger rate of fracture developments is related to lower amplitudes of porosity pulse as well as to lower durations of this pulse may control the production of hydrogen, as it would imply that there are different competing parameters regarding its production. Particularly, it may suggest that for H_2 production, the key parameters include not only the reaction kinetics but also the fracturing-related porosity pulses as well as the duration of this porosity pulse. The optimum combination of reaction kinetics, amplitude of porosity pulse, and duration of this porosity pulse may facilitate the migration of fluid as well as of native dihydrogen, resulting in the optimum production of dihydrogen that forms during serpentinization.

6. Conclusions

We have explored the micromechanics of reaction-induced fracturing due to mineral volumetric expansion during rock hydration. A numerical model based on the discrete element method was developed considering an Avrami type equation to simulate the volumetric expansion. The advancement of the hydration reaction depends on the nucleation and growth of fractures once the reaction starts. We applied our model to study the hydration of periclase to brucite as well as to the hydration of peridotite to serpentinite. For each case, the model can reproduce many of the experimental observations made by Zheng et al. (2018).

The influence of the stress on the reaction rate was first considered. The numerical model reproduced the volume increase, the sigmoidal shape of the reaction evolution, the formation of microfractures, and the existence of a transient porosity pulse observed by Zheng et al. (2018). We were also able to characterize the slow-down effect of the effective stress on the reaction rate. In the numerical model, the porosity increase was due to fracture opening while the subsequent porosity decrease was due to fracture clogging. The transition between these two regimes of porosity evolution occurred for a completion of reaction of about 30 to 40%. The amplitude of the porosity pulse measured in test peri1 was 2%, while it was equal to 12% in the numerical simulation that considered a propagation of a front, and 7% in the simulation that considered a pervasive reaction. The principal origin of the discrepancy between the numerical results and the experimental results might be related to the different boundary conditions used in both cases.

To model the serpentinization process, the influence of the temperature on the reaction rate was implemented in the model as an additional feature and was validated by reproducing the bell-shaped temperature—reaction rate relationships observed in experiments. In agreement with the experiments (Zheng et al., 2018; Zhu et al., 2016), the model could reproduce a porosity pulse at a completion of serpentinization reaction of about 35%. The alteration of material properties associated to the transformation of peridotite into serpentinite was also considered and tested. The results show that the reduction of the rock stiffness decreased slightly the amplitude of the porosity pulse by around 10%. Overall, material weakening does not significantly affect the reaction. For both periclase hydration and serpentinization reaction, a relationship between the amplitude of the porosity pulse, the duration of this porosity pulse and the rate of fracture development was characterized. The results indicate that a larger rate of fracture development is associated with a lower porosity pulse as well as with a shorter duration of this porosity pulse.

Applied to serpentinization process, our numerical model shows that a porosity pulse should form during the reaction and that the associated changes should modify the permeability evolution as well. These results indicate that the serpentinization progress is nonlinear in time and that the fluid flow through these reacting rocks should follow the same trend, either for water percolating into a partially serpentinized rock body or for hydrogen escaping this body. Moreover, the large stresses generated locally by hydration could promote shear and tensile failure, as observed in the microseismicity of geodynamical systems that undergo active serpentinization.

List of Symbols

Symbol	Designation	Unit
C	Extent of chemical reaction and transformation	None
t	Time	s
k	Kinetics parameter related to the rate of the reaction	None
n	Time exponent in Avrami equation	None
f	Kinetics rate parameter	None
T	Temperature	K
A	Preexponential factor of the reaction kinetics rate	None
E	Activation energy of reaction (specific to each mineral)	J/mol
R	Gas constant	$J{\cdot}K^{-1}{\cdot}mol^{-1}$
ΔG	Gibbs free energy of reaction	J/mol
m	Constant introduced in the rate law	None
T_0	Reference temperature	K
b	Parameter introduced to simplify the expression, with $b = \frac{E}{R}$	K
d	Parameter introduced to simplify the expression, with $d = \frac{m\ \Delta G}{R}$	K
γ_{int}	Coefficient of particle interaction range	None
F_n	Normal force	N
k_n	Normal stiffness	N/m
ΔD	Relative displacement between the interacting discrete elements	m
D	Distance between the centroids of interacting elements	m
D_{eq}	Initial equilibrium distance	m
E_{eq}	Local equivalent of the Young's modulus	Pa
R_a and R_b	Radii of two particles in contact	m
$F_{n,\max}$	Maximum acceptable normal force	N
t_p	Interparticle tensile strength	Pa
A_{int}	Interacting surface area between particles a and b	m^2
F_s	Shear force	N
Δu_s	Relative incremental tangential displacement	m
k_s	Local shear stiffness	N/m
μ	Local stiffness ratio	None
$F_{\text{s,max}}$	Maximum admissible shear force	N
c	Local cohesion between discrete elements	Pa
φ_b	Local frictional angle	°C
φ_c	Local residual frictional angle	°C
p_i	Local porosity of a particle	None
$V_{\text{s,i}}$	Volume of the spherical discrete element	m^3
$V_{\text{tt,i}}$	Total volume of the Voronoi cell i	m^3
m_p	Mass of a particle	kg
R_{inp}	Relative incremental local porosity	None
V_t	Volume of a particle at time t	m^3
$p_{V\text{exp}}$	Predefined overall percentage of volume expansion	None
V_{ini}	Initial volume of the particle	m^3
σ_m	Mean local stress of the particle	Pa
$\overline{\overline{\sigma}}$	Stress tensor	Pa
$\vec{x}^{i,k}$	Branch vector linking the particle center to a contact point	m
$\vec{f}^{i,k}$	Local contact force vector	N
γ	Weighting parameter for σ_m	Pa^{-1}
k_{ref}	Coefficient of kinetics parameter related to the rate of the reaction	None
t_0	Starting time of the growing process of the particle	s
t_c	Characteristic time used for normalization	Day or s
tc	Total duration of hydration experiments or numerical simulations	Hour or ms
t_{ndp}	Time duration of the porosity pulse within 50% of its peak value	s
$\sigma_i\ (i = 1,2,3)$	Local principal stresses of a particle	Pa
I_1	First invariant of the local stress tensor	Pa
$\sqrt{J_2}$	Square root of the second invariant of the local deviatoric stress tensor	Pa
X_{ini}	Initial value of a mechanical property of a particle	
X_{end}	Finial value of a mechanical property of a particle	
X'	Mechanical property of a reacted particle	

Acknowledgments

François Renard and Xiaojiao Zheng acknowledge funding from the Norwegian Research Council (project HADES, grant 250661). The authors thank Jess McBeck for providing a careful review of an early version of the present article. The authors thank Tim Wolterbeek and one anonymous reviewer who provided constructive reviews that helped improve the article. All the data and numerical boundary conditions used in the present study are given in the tables and the supporting information.

References

Avrami, M. (1939). Kinetics of phase change. I General theory. *The Journal of Chemical Physics*, *7*(12), 1103–1112. https://doi.org/10.1063/1.1750380

Bogdanov, Y., Sagalevitch, A., Chernyaev, E., Ashadze, A., Gurvich, E., Lukashin, V., et al. (1995). A study of the hydrothermal field at 14°45′N on the Mid-Atlantic Ridge using the "MIR" submersibles. BRIDGE newsl, 9, 9-13.

Cannat, M., Fontaine, F., & Escartín, J. (2010). Serpentinization and associated hydrogen and methane fluxes at slow spreading ridges. In *Diversity of Hydrothermal Systems on Slow Spreading Ocean Ridges*, (Vol. 188, pp. 241–264). Washington, D.C: American Geophysical Union. https://doi.org/10.1029/2008gm000760

Catalano, E., Chareyre, B., & Barthélémy, E. (2013). Pore-scale modeling of fluid-particles interaction and emerging poromechanical effects. *International Journal for Numerical and Analytical Methods in Geomechanics*, *38*(1), 51–71. https://doi.org/10.1002/nag.2198

Chareyre, B., Cortis, A., Catalano, E., & Barthélemy, E. (2011). Pore-scale modeling of viscous flow and induced forces in dense sphere packings. *Transport in Porous Media*, *92*(2), 473–493. https://doi.org/10.1007/s11242-011-9915-6

Charlou, J. L., Donval, J. P., Fouquet, Y., Jean-Baptiste, P., & Holm, N. (2002). Geochemistry of high H_2 and CH_4 vent fluids issuing from ultramafic rocks at the Rainbow hydrothermal field (36°14′N, MAR). *Chemical Geology*, *191*(4), 345–359. https://doi.org/10.1016/s0009-2541(02)00134-1

Chung, D.-H., Swica, J. J., & Crandall, W. B. (1963). Relation of single-crystal elastic Constants to polycrystalline isotropic elastic moduli of MgO. *Journal of the American Ceramic Society*, *46*(9), 452–457. https://doi.org/10.1111/j.1151-2916.1963.tb11775.x

Escartín, J., Hirth, G., & Evans, B. (1997). Nondilatant brittle deformation of serpentinites: Implications for Mohr-Coulomb theory and the strength of faults. *Journal of Geophysical Research*, *102*(B2), 2897–2913. https://doi.org/10.1029/96JB02792

Evans, O., Spiegelman, M., & Kelemen, P. B. (2018). A poroelastic model of serpentinization: Exploring the interplay between rheology, surface energy, reaction, and fluid flow. *Journal of Geophysical Research: Solid Earth*, *123*, 8653–8675. https://doi.org/10.1029/2017JB015214

Flatt, R. J. (2002). Salt damage in porous materials: How high supersaturations are generated. *Journal of Crystal Growth*, *242*(3-4), 435–454. https://doi.org/10.1016/s0022-0248(02)01429-x

Foustoukos, D. I., Savov, I. P., & Janecky, D. R. (2008). Chemical and isotopic constraints on water/rock interactions at the Lost City hydrothermal field, 30°N Mid-Atlantic Ridge. *Geochimica et Cosmochimica Acta*, *72*(22), 5457–5474. https://doi.org/10.1016/j.gca.2008.07.035

Früh-Green, G. L., Kelley, D. S., Bernasconi, S. M., Karson, J. A., Ludwig, K. A., Butterfield, D. A., et al. (2003). 30,000 Years of hydrothermal activity at the Lost City vent field. *Science*, *301*(5632), 495–498. https://doi.org/10.1126/science.1085582

Gratier, J.-P., Frery, E., Deschamps, P., Røyne, A., Renard, F., Dysthe, D., et al. (2012). How travertine veins grow from top to bottom and lift the rocks above them: The effect of crystallization force. *Geology*, *40*(11), 1015–1018. https://doi.org/10.1130/g33286.1

Guélard, J., Beaumont, V., Rouchon, V., Guyot, F., Pillot, D., Jézéquel, D., et al. (2017). Natural H_2 in Kansas: Deep or shallow origin? *Geochemistry, Geophysics, Geosystems*, *18*, 1841–1865. https://doi.org/10.1002/2016GC006544

Guillot, S., Schwartz, S., Reynard, B., Agard, P., & Prigent, C. (2015). Tectonic significance of serpentinites. *Tectonophysics*, *646*, 1–19. https://doi.org/10.1016/j.tecto.2015.01.020

Horning, G., Sohn, R. A., Canales, J. P., & Dunn, R. A. (2018). Local seismicity of the Rainbow Massif on the Mid-Atlantic Ridge. *Journal of Geophysical Research: Solid Earth*, *123*, 1615–1630. https://doi.org/10.1002/2017JB015288

Iyer, K., Jamtveit, B., Mathiesen, J., Malthe-Sørenssen, A., & Feder, J. (2008). Reaction-assisted hierarchical fracturing during serpentinization. *Earth and Planetary Science Letters*, *267*(3-4), 503–516. https://doi.org/10.1016/j.epsl.2007.11.060

Jamtveit, B., Malthe-Sørenssen, A., & Kostenko, O. (2008). Reaction enhanced permeability during retrogressive metamorphism. *Earth and Planetary Science Letters*, *267*(3-4), 620–627. https://doi.org/10.1016/j.epsl.2007.12.016

Jamtveit, B., Putnis, C. V., & Malthe-Sørenssen, A. (2008). Reaction induced fracturing during replacement processes. *Contributions to Mineralogy and Petrology*, *157*(1), 127–133. https://doi.org/10.1007/s00410-008-0324-y

Kelemen, P. B., & Hirth, G. (2012). Reaction-driven cracking during retrograde metamorphism: Olivine hydration and carbonation. *Earth and Planetary Science Letters*, *345-348*, 81–89. https://doi.org/10.1016/j.epsl.2012.06.018

Kelley, D. S., Karson, J. A., Früh-Green, G. L., Yoerger, D. R., Shank, T. M., Butterfield, D. A., et al. (2005). A serpentinite-hosted ecosystem: The Lost City hydrothermal field. *Science*, *307*(5714), 1428–1434. https://doi.org/10.1126/science.1102556

Kozicki, J., & Donzé, F. V. (2008). A new open-source software developed for numerical simulations using discrete modeling methods. *Computer Methods in Applied Mechanics and Engineering*, *197*(49-50), 4429–4443. https://doi.org/10.1016/j.cma.2008.05.023

Kozicki, J., & Donzé, F. V. (2009). YADE-OPEN DEM: An open-source software using a discrete element method to simulate granular material. *Engineering Computations*, *26*(7), 786–805. https://doi.org/10.1108/02644400910985170

Lafay, R., Montes-Hernandez, G., Renard, F., & Vonlanthen, P. (2018). Intracrystalline reaction-induced cracking in olivine evidenced by hydration and carbonation experiments. *Minerals*, *8*(9), 412. https://doi.org/10.3390/min8090412

Larin, N., Zgonnik, V., Rodina, S., Deville, E., Prinzhofer, A., & Larin, V. N. (2014). Natural molecular hydrogen seepage associated with surficial, rounded depressions on the European craton in Russia. *Natural Resources Research*, *24*(3), 369–383. https://doi.org/10.1007/s11053-014-9257-5

Larin, N.V., Larin, V.N., & Gorbatikov A.V. (2010). Circular structures, caused by the deep seeping of hydrogen. Degassing of the Earth: Geotectonics, geodynamics, deep fluids, oil and gas; hydrocarbons and life. Russian Conference with International Participation Dedicated to the 100th Anniversary of Academician P.N. Kropotkin, p. 282 (in Russian).

Lasaga, A. C. (1981). Transition state theory. In A. C. Lasaga, & R. J. Kirkpatrick (Eds.), *Kinetics of geochemical processes*, (pp. 135–169). Washington, D. C.: Mineralogical Society of America. https://doi.org/10.1515/9781501508233-008

Lasaga, A. C. (1986). Metamorphic reaction rate laws and development of isograds. *Mineralogical Magazine*, *50*(357), 359–373. https://doi.org/10.1180/minmag.1986.050.357.02

Lasaga, A. C. (1995). Fundamental approaches in describing mineral dissolution and precipitation rates. In A. F. White, & S. L. Brantley (Eds.), *Chemical Weathering Rates of Silicate Minerals*, (pp. 23–86). Washington, D. C.: Mineralogical Society of America. https://doi.org/10.1515/9781501509650-004

Lisabeth, H. P., Zhu, W., Kelemen, P. B., & Ilgen, A. (2017). Experimental evidence for chemo-mechanical coupling during carbon mineralization in ultramafic rocks. *Earth and Planetary Science Letters*, *474*, 355–367. https://doi.org/10.1016/j.epsl.2017.06.045

Lobo-Guerrero, S., & Vallejo, L. E. (2006). Discrete element method analysis of railtrack ballast degradation during cyclic loading. *Granular Matter*, *8*(3-4), 195–204. https://doi.org/10.1007/s10035-006-0006-2

Lyer, K., Austrheim, H., John, T., & Jamtveit, B. (2008). Serpentinization of the oceanic lithosphere and some geochemical consequences: Constraints from the Leka Ophiolite Complex, Norway. *Chemical Geology*, *249*(1-2), 66–90. https://doi.org/10.1016/j.chemgeo.2007.12.005

MacDonald, A. H., & Fyfe, W. S. (1985). Rate of serpentinization in seafloor environments. *Tectonophysics*, *116*(1-2), 123–135. https://doi.org/10.1016/0040-1951(85)90225-2

Malvoisin, B., Brantut, N., & Kaczmarek, M.-A. (2017). Control of serpentinisation rate by reaction-induced cracking. *Earth and Planetary Science Letters*, *476*, 143–152. https://doi.org/10.1016/j.epsl.2017.07.042

Malvoisin, B., Brunet, F., Carlut, J., Rouméjon, S., & Cannat, M. (2012). Serpentinization of oceanic peridotites: 2. Kinetics and processes of San Carlos olivine hydrothermal alteration. *Journal of Geophysical Research*, *117*, B04102. https://doi.org/10.1029/2011JB008842

Marcaillou, C. (2011). Serpentinisation et production d'hydrogène en contexte de dorsale lente: approche expérimentale et numérique (Doctoral dissertation, Université de Grenoble).

Marcaillou, C., Muñoz, M., Vidal, O., Parra, T., & Harfouche, M. (2011). Mineralogical evidence for H_2 degassing during serpentinization at 300°C/300 bar. *Earth and Planetary Science Letters*, *303*(3-4), 281–290. https://doi.org/10.1016/j.epsl.2011.01.006

Martin, B., & Fyfe, W. S. (1970). Some experimental and theoretical observations on the kinetics of hydration reactions with particular reference to serpentinization. *Chemical Geology*, *6*, 185–202. https://doi.org/10.1016/0009-2541(70)90018-5

McCollom, T. M., & Bach, W. (2009). Thermodynamic constraints on hydrogen generation during serpentinization of ultramafic rocks. *Geochimica et Cosmochimica Acta*, *73*(3), 856–875. https://doi.org/10.1016/j.gca.2008.10.032

Moody, J. B. (1976). Serpentinization: A review. *Lithos*, *9*(2), 125–138. https://doi.org/10.1016/0024-4937(76)90030-x

Nicot, F., Hadda, N., Guessasma, M., Fortin, J., & Millet, O. (2013). On the definition of the stress tensor in granular media. *International Journal of Solids and Structures*, *50*(14-15), 2508–2517. https://doi.org/10.1016/j.ijsolstr.2013.04.001

Noiriel, C., Steefel, C. I., Yang, L., & Ajo-Franklin, J. (2012). Upscaling calcium carbonate precipitation rates from pore to continuum scale. *Chemical Geology*, *318-319*, 60–74. https://doi.org/10.1016/j.chemgeo.2012.05.014

O'Hanley, D. S. (1992). Solution to the volume problem in serpentinization. *Geology*, *20*(8), 705–708. https://doi.org/10.1130/0091-7613(1992)020<0705:STTVPI>2.3.CO;2

Plümper, O., Beinlich, A., Bach, W., Janots, E., & Austrheim, H. (2014). Garnets within geode-like serpentinite veins: Implications for element transport, hydrogen production and life-supporting environment formation. *Geochimica et Cosmochimica Acta*, *141*, 454–471. https://doi.org/10.1016/j.gca.2014.07.002

Plümper, O., Røyne, A., Magrasó, A., & Jamtveit, B. (2012). The interface-scale mechanism of reaction-induced fracturing during serpentinization. *Geology*, *40*(12), 1103–1106. https://doi.org/10.1130/g33390.1

Proskurowski, G., Lilley, M. D., Seewald, J. S., Fruh-Green, G. L., Olson, E. J., Lupton, J. E., et al. (2008). Abiogenic hydrocarbon production at Lost City hydrothermal field. *Science*, *319*(5863), 604–607. https://doi.org/10.1126/science.1151194

Røyne, A., Jamtveit, B., Mathiesen, J., & Malthe-Sørenssen, A. (2008). Controls on rock weathering rates by reaction-induced hierarchical fracturing. *Earth and Planetary Science Letters*, *275*(3-4), 364–369. https://doi.org/10.1016/j.epsl.2008.08.035

Schlindwein, V., & Schmid, F. (2016). Mid-ocean-ridge seismicity reveals extreme types of ocean lithosphere. *Nature*, *535*(7611), 276–279. https://doi.org/10.1038/nature18277

Scholtès, L., & Donzé, F.-V. (2013). A DEM model for soft and hard rocks: Role of grain interlocking on strength. *Journal of the Mechanics and Physics of Solids*, *61*(2), 352–369. https://doi.org/10.1016/j.jmps.2012.10.005

Skarbek, R. M., Savage, H. M., Kelemen, P. B., & Yancopoulos, D. (2018). Competition between crystallization-induced expansion and creep compaction during gypsum formation, and implications for serpentinization. *Journal of Geophysical Research: Solid Earth*, *123*, 5372–5393. https://doi.org/10.1029/2017JB015369

Šmilauer, V. Catalano, E., & Chareyre, B. (2015), Yade documentation 2nd ed. The Yade Project DOI https://doi.org/10.5281/zenodo.34073 (http://yade-dem.org/doc/).

Spriggs, R. M., Brissette, L. A., & Vasilos, T. (1962). Effect of porosity on elastic and shear moduli of polycrystalline magnesium oxide. *Journal of the American Ceramic Society*, *45*(8), 400–400. https://doi.org/10.1111/j.1151-2916.1962.tb11180.x

Steiger, M. (2005). Crystal growth in porous materials—II: Influence of crystal size on the crystallization pressure. *Journal of Crystal Growth*, *282*(3-4), 470–481. https://doi.org/10.1016/j.jcrysgro.2005.05.008

Ulven, O. I., Jamtveit, B., & Malthe-Sørenssen, A. (2014). Reaction-driven fracturing of porous rock. *Journal of Geophysical Research: Solid Earth*, *119*, 7473–7486. https://doi.org/10.1002/2014JB011102

Ulven, O. I., Storheim, H., Austrheim, H., & Malthe-Sørenssen, A. (2014). Fracture initiation during volume increasing reactions in rocks and applications for CO_2 sequestration. *Earth and Planetary Science Letters*, *389*, 132–142. https://doi.org/10.1016/j.epsl.2013.12.039

Van Noort, R., Wolterbeek, T., Drury, M., Kandianis, M., & Spiers, C. (2017). The Force of crystallization and fracture propagation during in-situ carbonation of peridotite. *Minerals*, *7*(10), 190. https://doi.org/10.3390/min7100190

Wegner, W. W., & Ernst, W. G. (1983). Experimentally determined hydration and dehydration reaction rates in the system MgO-SiO2-H2O. *American Journal of Science*, *283-A*, 151–180.

Wolterbeek, T. K. T., van Noort, R., & Spiers, C. J. (2017). Reaction-driven casing expansion: potential for wellbore leakage mitigation. *Acta Geotechnica*. https://doi.org/10.1007/s11440-017-0533-5

Zheng, X., Cordonnier, B., Zhu, W., Renard, F., & Jamtveit, B. (2018). Effects of confinement on reaction-induced fracturing during hydration of periclase. *Geochemistry, Geophysics, Geosystems.*, *19*, 2661–2672. https://doi.org/10.1029/2017GC007322

Zhu, W., Fusseis, F., Lisabeth, H., Xing, T., Xiao, X., De Andrade, V., & Karato, S. (2016). Experimental evidence of reaction-induced fracturing during olivine carbonation. *Geophysical Research Letters*, *43*, 9535–9543. https://doi.org/10.1002/2016GL070834